

WOCS 40007: A Detached Eclipsing Binary near the Turnoff of the Open Cluster NGC 6819¹

Mark W. Jeffries, Jr.²; Eric L. Sandquist²; Robert D. Mathieu^{3,11}; Aaron M. Geller^{3,4,11}; Jerome A. Orosz²; Katelyn E. Milliman^{3,11}; Lauren N. Brewer²; Imants Platais⁵; Karsten Brogaard^{6,7}; Frank Grundahl⁷; Soeren Frandsen⁷; Aaron Dotter^{8,9}; Dennis Stello¹⁰

ABSTRACT

We analyze extensive BVR_cI_c time-series photometry and radial-velocity measurements for WOCS 40007 (Auner 259; KIC 5113053), a double-lined detached eclipsing binary and a member of the open cluster NGC 6819. Utilizing photometric observations from the 1-meter telescope at Mount Laguna Observatory and spectra from the WIYN 3.5-meter telescope, we measure precise and

²San Diego State University, Department of Astronomy, San Diego, CA, 92182; jeffries@sciences.sdsu.edu; erics@mintaka.sdsu.edu; orosz@sciences.sdsu.edu; lbrewer@rohan.sdsu.edu

³University of Wisconsin-Madison, Department of Astronomy, Madison, WI, 53706; mathieu@astro.wisc.edu; milliman@astro.wisc.edu

⁴Center for Interdisciplinary Exploration and Research in Astrophysics (CIERA) & Dept. of Physics and Astronomy, Northwestern University, 2145 Sheridan Road, Evanston, IL 60208 a-geller@northwestern.edu

⁵Department of Physics and Astronomy, The Johns Hopkins University, Baltimore, MD 21218, USA ; imants@pha.jhu.edu

⁶Department of Physics & Astronomy, University of Victoria, P.O. Box 3055, Victoria, BC V8W 3P6, Canada

⁷Department of Physics and Astronomy, Aarhus University, Ny Munkegade 120, 8000 Aarhus C, Denmark; kfb@phys.au.dk, fgj@phys.au.dk, srf@phys.au.dk

⁸Research School of Astronomy and Astrophysics, The Australian National University, Canberra, ACT, Australia; aaron.dotter@gmail.com

⁹Space Telescope Science Institute, 3700 San Martin Drive, Baltimore, MD, 21218

¹⁰Sydney Institute for Astronomy (SIfA), School of Physics, University of Sydney, NSW, 2006, Australia; stello@physics.usyd.edu.au

¹¹Visiting Astronomer, Kitt Peak National Observatory, National Optical Astronomy Observatories, which is operated by the Association of Universities for Research in Astronomy, Inc. (AURA) under cooperative agreement with the National Science Foundation.

accurate masses ($\sim 1.6\%$ uncertainty) and radii ($\sim 0.5\%$) for the binary components. In addition, we discover a third star orbiting the binary with a period greater than 3000 days using radial velocities and *Kepler* eclipse timings.

Because the stars in the eclipsing binary are near the cluster turnoff, they are evolving rapidly in size and are sensitive to age. With a metallicity of $[\text{Fe}/\text{H}] = +0.09 \pm 0.03$, we find the age of NGC 6819 to be about 2.4 Gyr from CMD isochrone fitting and 3.1 ± 0.4 Gyr by analyzing the mass-radius ($M - R$) data for this binary. The $M - R$ age is above previous determinations for this cluster, but consistent within 1σ uncertainties. When the $M - R$ data for the primary star of the additional cluster binary WOCS 23009 is included, the weighted age estimate drops to 2.5 ± 0.2 Gyr, with a systematic uncertainty of at least 0.2 Gyr. The age difference between our CMD and $M - R$ findings may be the result of systematic error in the metallicity or helium abundance used in models, or due to slight radius inflation of one or both stars in the WOCS 40007 binary.

Subject headings: open clusters and associations: individual (NGC 6819) - stars: evolution - stars: binaries: spectroscopic - stars: binaries: eclipsing - techniques: spectroscopy - techniques: photometry

1. Introduction

Detached eclipsing binaries (DEBs) provide a means of deriving precise stellar ages while avoiding most of the major systematic errors in isochrone fits that are introduced by uncertainties in model assumptions, reddening, distance, and color-temperature transformations (Andersen 1991; Torres et al. 2010). The masses and radii of the stellar components in such a binary make a *direct* comparison possible with stellar evolution theory if chemical composition is known independently. The characteristics of the stars (especially radius) will also have sensitivity to age if one or both of the stars has evolved significantly away from the main sequence. If an eclipsing binary containing such an evolved star can be found in a star cluster, it can place tight constraints on the age of *all* of the cluster stars.

With the start of NASA’s *Kepler* mission, star clusters within its field of view are becoming important test beds for stellar evolution theories. *Kepler* has discovered previously unknown eclipsing binary systems both in the field (Prša et al. 2011; Slawson et al. 2011) and in

¹This is paper 56 of the WIYN Open Cluster Study (WOCS).

open clusters (e.g., Sandquist et al. 2013). As the population of binary members with known masses and radii increases, it will be possible to statistically improve the binary star constraint on cluster ages derived from the mass-radius ($M - R$) plane. Additionally, a well-populated $M - R$ plane observationally constrains difficult-to-measure cluster parameters, such as He abundance, when analyzed together with a cluster CMD (Grundahl et al. 2008; Brogaard et al. 2011, 2012).

NGC 6819 is a rich open cluster in the *Kepler* field that has been well studied. Hole et al. (2009) completed the first comprehensive kinematic membership study as a part of the WIYN Open Cluster Study (WOCS; Mathieu 2000), including stars from the upper main sequence (MS) to the giant branch. Several previous studies of the color-magnitude diagram (CMD; Burkhead 1971; Lindoff 1972; Auner 1974; Rosvick & Vandenberg 1998; Kalirai et al. 2001; Kalirai & Tosi 2004) have produced age estimates between about 2.0 and 2.5 Gyr. More recently, Basu et al. (2011) used asteroseismic data from *Kepler* to constrain characteristics of red giant branch stars and to place a constraint on the cluster distance and age. They find $(m - M)_0 = 11.85 \pm 0.05$ and an age of 2.1 – 2.5 Gyr.

Our group has undertaken a program to analyze eclipsing binary stars in this cluster, and to improve the determination of its age using the *ensemble* of eclipsing systems. In our first paper (Sandquist et al. 2013), we analyzed the long-period binary WOCS 23009 (Auner 851), which contains the most evolved star known to eclipse in this cluster. Here we focus on the binary system WOCS 40007 (Auner 259; $\alpha_{2000} = 19^{\text{h}}41^{\text{m}}33^{\text{s}}.94$, $\delta_{2000} = +40^{\circ}13'00''.5$), which was discovered and classified as a DEB by Talamantes et al. (2010). WOCS 40007 contains stars that are less evolved than the primary star in WOCS 23009, and so they are less age sensitive. However, both stars can contribute to the determination of the cluster age, and they also allow us to measure the characteristics of stars of other masses in the cluster. This study uses extensive ground-based photometric and radial-velocity (RV) observations to characterize the binary, and *Kepler* photometry to monitor eclipse timing and examine out-of-eclipse variations.

Section 2 contains a discussion of the metallicity, reddening, and distance of NGC 6819. A discussion of the photometric and spectroscopic observations of the binary star, as well as the reduction and modeling of the data, is described in §3. In §4 we present our photometric and spectroscopic results for the components of WOCS 40007. Finally, we determine the age for NGC 6819 and discuss our results in §5.

2. Physical Parameters of NGC 6819

Before describing the observations, we review important external information that goes into later analysis: metallicity, reddening, and distance.

2.1. Metallicity

Uncertainty in the metallicity of cluster stars potentially produces one of the biggest systematic uncertainties in age via the theoretical prediction of radii. Friel et al. (1989) first determined the metallicity of NGC 6819 with a study of moderate-resolution spectra of giant stars and found $[\text{Fe}/\text{H}] = -0.1$. Later work with the same spectroscopic data led Friel & Janes (1993) to derive $[\text{Fe}/\text{H}] = +0.05 \pm 0.11$. However, both of these results are dependent on the assumed reddening of the system and on data that the authors acknowledged to be of high uncertainty. Twarog et al. (1997) found $[\text{Fe}/\text{H}] = +0.07 \pm 0.05$ using the data of Friel & Janes (1993), but with an independent estimate of the cluster reddening. More recently, Bragaglia et al. (2001) used high-dispersion spectra of three red clump stars to derive the cluster metallicity and element-to-element abundances for NGC 6819. They found that their targets possess abundance ratios quite close to solar values except for a small excess of silicon and large overabundance of sodium. Bragaglia et al. (2001) find the cluster to be slightly more metal-rich than the Sun with $[\text{Fe}/\text{H}] = +0.09 \pm 0.03$. To date, the Bragaglia et al. (2001) value is the only published metallicity using high resolution spectra, and so we use this as our preferred value in the subsequent analysis. Although NGC 6819 is part of a larger homogeneous study of open cluster abundances (Bragaglia 2008), there has not yet been a systematic comparison of their abundances with previous measurements in well-studied clusters. As a result, we have to allow for the possibility of a systematic error in $[\text{Fe}/\text{H}]$ that could be larger than the quoted uncertainty in the mean.

2.2. Reddening and Distance

Previously quoted reddening values in the literature range from $E(B - V) = 0.12$ (Burkhead 1971), 0.30 (Lindoff 1972), 0.28 (Auner 1974), 0.15 (Canterna et al. 1986), and 0.142 ± 0.044 (Bragaglia et al. 2001). In the most recent study, Bragaglia et al. (2001) derived the cluster reddening by determining the temperatures of 3 bright red clump stars from line excitation (a reddening-free parameter) and then comparing the observed color of each star with values predicted by theoretical models. It should be noted that one of the stars observed by Bragaglia et al. is a binary (Auner 1979; Hole et al. 2009), and so its contribution is suspect.

In order to make the most reliable comparisons between results from the color-magnitude diagram and from the components of WOCS 40007 (which are independent of distance and reddening), we redetermine the reddening here.

To compute the reddening, we used a method based on Grocholski & Sarajedini (2002), comparing the median red clump photometry of NGC 6819 with that of M67, a cluster with low and well-determined reddening ($E(B - V) = 0.041 \pm 0.004$; Taylor 2007) and distance modulus ($(m - M)_V = 9.72 \pm 0.05$, $(m - M)_0 = 9.60 \pm 0.03$; Sandquist 2004). M67 and NGC 6819 also have similar ages and metallicities that fall in a regime where variations in those quantities have modest effects on the brightness of the red clump. The metallicity difference $\Delta[\text{Fe}/\text{H}] = 0.09$ is theoretically expected to affect the clump magnitude at only the 0.01 level in 2MASS infrared filters, but has a larger effect towards bluer wavelengths (Girardi & Salaris 2001), reaching almost 0.1 mag in B . The ~ 1.5 Gyr age difference between the two clusters implies that the M67 red clump should be fainter in all filters — approximately 0.07 mag in 2MASS filters and increasing to about 0.14 mag in B (Girardi & Salaris 2001; Grocholski & Sarajedini 2002). As a result, for these two clusters the age and metallicity effects are theoretically expected to partially compensate for each other, so that there is a nearly constant magnitude offset in all filters. Based on these considerations, we can use the magnitude of the red clump stars in different filter bands to seek a simultaneous solution for the difference in the cluster distance moduli $\Delta(m - M)_0$ and difference in optical depth to the clusters $\Delta\tau_1$ if an extinction law is assumed. The difference in distance moduli is mostly set by magnitude differences in the infrared where extinction effects are small, while the difference in optical depth is determined by how the magnitude differences change from filter to filter.

We used BVI_c (Talamantes et al. 2010 for NGC 6819, and Sandquist 2004 for M67) and JHK_s photometry (Skrutskie et al. 2006, 2MASS) for clump stars. In NGC 6819, we restrict the sample to single-star members as identified in Hole et al. (2009) and also eliminated likely evolved clump stars identified from asteroseismology (Corsaro et al. 2012). We also employ the York Extinction Solver² (McCall 2004) to calculate the reddening and extinctions in different filters, assuming that the clump stars are approximately K0 III giants. We are able to get a consistent solution for all filter bands with $\Delta(m - M)_0 = 2.40^{+0.03}_{-0.02}$ and $\Delta\tau_1 = 0.088 \pm 0.032$. The uncertainties depend mostly on the uncertainties in the *relative* abundance of M67 and NGC 6819, which we estimate to be about 0.05 dex. This estimate is based on the work of Friel & Janes (1993), which is the only spectroscopic study to measure the metallicity of NGC 6819 and M67 in a consistent way that would minimize systematic

²<http://www2.cadc-ccda.hia-ihp.nrc-cnrc.gc.ca/community/YorkExtinctionSolver/>

errors. This study found a difference of 0.14 dex, with NGC 6819 being the more metal-rich cluster. After accounting for M67’s distance and reddening, we get $(m - M)_0 = 12.00 \pm 0.05$, $(m - M)_V = 12.37 \pm 0.10$ and $E(B - V) = 0.12 \pm 0.03$ for dwarf stars near the turnoff of NGC 6819. Figure 1 illustrates the consistency in median red clump magnitudes between the two clusters in BVI_cJHK_s as a function of wave number ($1/\lambda$) when incorporating these shifts.

The reddening is at the low end of the range of previous determinations (Bragaglia et al. 2001; Canterna et al. 1986; Burkhead 1971). Our value for the apparent distance modulus agrees with the measurements by Rosvick & Vandenberg (1998, $(m - M)_V \approx 12.35$) and Kalirai et al. (2001, $(m - M)_V = 12.30 \pm 0.12$), although larger than the recent asteroseismic value determined by Basu et al. (2011, $(m - M)_0 = 11.85 \pm 0.05$) using a reddening $E(B - V) = 0.15$. Figure 2 shows the consistency between the MS and clumps in the resulting corrected CMDs of NGC 6819 and M67. We also note that the turnoff of M67 is fainter and redward of the NGC 6819 turnoff, indicating that NGC 6819 is younger, as expected. We will discuss independent distance moduli derived from the eclipsing binary stars in §4.3.

3. Observations and Data Reduction

3.1. Photometry

We obtained CCD images in B , V , R_c , and I_c of NGC 6819 using the 1-m telescope at Mount Laguna Observatory (hereafter, MLO). The CCD 2005 camera covers $13.7' \times 13.7'$ on the sky, resulting in a scale of $0''.41$ per pixel. Our photometric dataset consists of 46 nights between March 2001 and September 2011, with the majority from 2008, 2010, and 2011. The dataset includes images presented by Talamantes et al. (2010) that were taken with the same telescope and camera combination. A list of additional nights of photometry is in Table 1.

Our data reduction pipeline uses *IRAF*³ routines for overscan and bias subtraction, and flat fielding. Our science images are flat-field corrected using images acquired during the twilight of each night, although for a few nights we use a flat-field image composed from dome and twilight flats, as noted by a superscript “b” in Table 1.

We use a slightly modified version of the image subtraction package ISIS (Alard 2000) to

³*IRAF* is distributed by the National Optical Astronomy Observatory, which is operated by the Association of Universities for Research in Astronomy, Inc., under cooperative agreement with the National Science Foundation.

make photometric measurements, as described in Sandquist, Serio, & Shetrone (2011) and Talamantes et al. (2010). In short, we improved the handling of image alignment, fixed an error in the uncertainty determination, and modified how ISIS acquires the reference flux in a crowded field. Using ISIS, we interpolate our B , V , R_c , and I_c data sets to a common coordinate system. Reference images are made for each filter from about 20 of the best seeing images, and these were subtracted from individual science images after being convolved to match the seeing.

The output of ISIS is a measurement of the difference flux from the subtracted images. The ISIS aperture photometry routine uses a circular aperture of `radphot` pixels, weighted by the point-spread function and normalized to a larger aperture with a radius of `rad_aper` pixels. For our MLO datasets, we set `radphot` = 4 and `rad_aper` = 7. The magnitude of the binary in each frame is calculated using the difference flux from the subtracted image and a flux measured on the unsubtracted reference image.

Since accurate eclipse depths are critical in the characterization of an eclipsing binary, we checked the ISIS eclipse depths by measuring the eclipse depth for a primary eclipse on a single night using a traditional curve-of-growth analysis (Stetson 1990). We used the *MATCH* and *MASTER* tasks to remove zero-point differences between images introduced by variations in atmospheric transparency, airmass, and exposure time. We found that the derived eclipse depth from ISIS and the curve of growth analysis were identical within the uncertainties.

Figure 3 shows our full set of ground-based photometric observations phased to the orbital period, and Figure 4 is zoomed in on the primary and secondary eclipses, showing the observations near eclipse minima that were used to model the binary.

3.2. Spectra

Spectroscopic observations were obtained as part of the WIYN Open Cluster Study (WOCS; Mathieu 2000). We use the observations of Hole et al. (2009), who presented high-precision RVs for 1207 stars in NGC 6819, and more recent WOCS spectroscopic observations of Milliman et al. (2013). A detailed explanation of the acquisition and reduction of the spectra, and the RV measurement uncertainties (typically, $\sigma = 0.5 \text{ km s}^{-1}$ for single stars) of WOCS observations can be found in Geller et al. (2008); below we provide a brief description.

WOCS uses the WIYN⁴ 3.5-m telescope on Kitt Peak and the Hydra multi-object spec-

⁴The WIYN Observatory is a joint facility of the University of Wisconsin-Madison, Indiana University,

trograph (MOS) instrument, which is a fiber-fed spectrograph capable of obtaining about 80 spectra simultaneously (usually 10 fibers to measure the sky, and about 70 fibers observing stars). We observed NGC 6819 over 35 separate observing runs using the echelle grating, which provides a spectral resolution of $\sim 15 \text{ km s}^{-1}$. The spectra are centered at 513 nm with a 25 nm range in order to cover narrow absorption lines around the Mg I b triplet. Spectroscopic observations of WOCS 40007 were completed using 1- or 2-hour integrations per visit that were split into three separate integrations to allow for the rejection of cosmic rays.

Standard spectroscopic image processing was also done within *IRAF*. Calibration of the spectra from each epoch used one associated 200 s flat field and two 300 s ThAr emission lamp spectra bracketing science integrations. RVs for WOCS 40007 were extracted using Two Dimensional CORrelation (TODCOR; Zucker & Mazeh 1994) against an observed solar template spectrum. Additionally, we correct for fiber-to-fiber radial-velocity offsets present in the Hydra MOS, as described in Geller et al. (2008). The offsets ranged from -0.70 to 0.37 km s^{-1} , with an rms value of 0.16 km s^{-1} .

For the purposes of this paper, we have not attempted to estimate the impact of lines moving into or out of the spectroscopic window. Meibom et al. (2009) examined this effect for a binary in NGC 188 for the exact same instrument and setup, finding that it had an effect of up to 3 km s^{-1} near primary eclipse and the systematic error was phase dependent. However, at most phases the systematic errors were less than 1 km s^{-1} . Figure 5 shows our RV observations phased over the binary orbit, along with the velocity residuals (observed minus computed). In addition to the three observations we omitted due to potential effects of eclipses, there are three measurement epochs that show significant deviations from the model. We will address the issue of spectral window corrections in a future paper.

3.3. Binary Component Magnitudes and Temperatures

Before modeling the spectroscopic and photometric data, we first derive constraints on the temperatures of the individual stars.

To derive spectroscopic temperatures, we first selected the 22 spectra where the primary and secondary are well separated in RV space, as this reduces complications involving blended lines. We selected templates from a library of ATLAS9 synthetic spectra (Castelli & Kurucz 2003, 2004) calculated by Jon Morse for an extensive grid of model atmospheres computed

using the ATLAS9 code developed by Kurucz, originally for the CfA Digital Speedometers (e.g. Latham et al. 2002) and broadened to the WIYN spectral resolution. The templates were chosen to have $\log(g) = 4.0$ and T_{eff} in a range from 3500 K to 7000 K (in steps of 250 K). Non-rotating templates were chosen because we were unable to identify significant rotational broadening in the spectra. For each observation we cross-correlated all combinations of these templates against the observed spectrum using TODCOR, and determined the template combination that returned the highest 2D correlation peak height. This analysis returned temperatures of 6350 ± 150 K for the primary component and 5930 ± 150 K for the secondary. The standard error in the mean from the 22 spectra was 80 K, but we have increased the uncertainty to 150 K to account for the possibility of a systematic offset in temperature when correlating observed spectra against synthetic templates (e.g. Meibom et al. 2009).

We also have standard-system photometry of WOCS 40007 in B , V , and I_c from Talamantes et al. (2010) that can be used to derive photometric temperatures. (R_c was not calibrated.) The calibrated observations were taken on a single night, which unfortunately was the night of a primary eclipse. Three to four observations per filter were taken outside of eclipse, but these may still be systematically faint by approximately 0.01 mag because they were not at quadrature when the system light is maximum.

The discovery of a faint tertiary star (see §3.5) adds a complication to the disentanglement of the light of the stars, but because the secondary eclipse is total, the photometry of the secondary star is well constrained. To derive the photometry of the primary star, we need to make the assumptions about the photometric properties of the tertiary star. At present, the tertiary’s photometry is weakly constrained by the assumption that it falls on the cluster fiducial line in the CMD, and by the minimum mass derived in §3.5 (which sets a lower limit on the brightness of the tertiary). The need to have the primary star fall on the cluster fiducial line puts an effective upper limit on how bright the tertiary can be. The measured secondary eclipse depths (Δm_s) and corresponding magnitudes of each component are listed in Table 2. We find the uncertainties for the secondary eclipse depth by determining the interquartile range of measurements during totality and propagate this through the calculations to determine the magnitude uncertainties.

As seen in Figure 6 (c) and (e), the photometry of the primary component of WOCS 40007 is consistent with the main sequence line in both $B - V$ and $V - I_c$ for an appropriate choice of tertiary in the CMD, but the secondary component is only consistent with the main sequence in $B - V$. In $V - I_c$, the secondary is redder than the main sequence by ~ 0.06 mag. Since the secondary eclipse is total, the properties of the secondary component are independent of the assumptions about the tertiary. This is true as long as the eclipse depths and system photometry are measured correctly. Because this shift in $V - I_c$ affects

the determination of the temperature of the secondary star, we delve a little into possible causes. We first compared our photometry to that of previous studies. Only Rosvick & Vandenberg (1998) and Hole et al. (2009) have previously presented I_c photometry, and in both cases, WOCS 40007 is shifted similarly to the red *relative to the main sequence in the same dataset*.

Using the secondary eclipse depths to decompose the system photometry, we still find that the secondary star is redder than the main sequence at the same brightness level. Looking at B and V photometry from these sources as well as Kalirai et al. (2001), the position of the secondary star in the CMD is much more consistent with the main sequence (see Fig. 6).

Because WOCS 40007 contains a relatively short period binary, we considered the possibility of photometric variations due to spots and stellar activity. We detect non-synchronous spot modulation at about the 1% level outside of eclipse in *Kepler* photometry, but due to systematic trends introduced by *Kepler*, longer timescale variations are harder to study reliably. NGC 6819 was observed at different epochs in previously published datasets, so that longer term photometric variations might be identifiable if large enough. To produce clearer comparisons with our photometry, we corrected the respective datasets for zero-point differences determined from all stars in common. There are often significant zeropoint offsets between datasets (see Table 3), but there is only evidence of problematic color-dependent trends in the B photometry of Hole et al.. The results from the decomposition of the photometry from each source are given in Table 2. The differences cover a range of up to 0.07 mag (in B) in brightness and 0.05 (in $B - V$) in color and are similar to twice the semi-interquartile ranges in the photometry comparisons (Table 3).

At present we do not have a satisfying explanation for the unusual $V - I_c$ color of the secondary star. Because of potential issues with the I_c photometry, we will focus on the isochrone fit in the $(V, B - V)$ CMD (see Section 5.1.1). In order to constrain the temperature of each component, we adopt the metallicity $[\text{Fe}/\text{H}] = +0.09 \pm 0.03$ from Bragaglia et al. (2001) and use our value for the cluster reddening (see §2.2) and the empirical temperature scale of Casagrande et al. (2010). Vandenberg et al. (2010) employed this temperature scale to transform their theoretical models to the color-magnitude plane, and found that it produced excellent agreement with the photometry of stars similar to NGC 6819’s upper MS stars in well-measured open clusters with solar (M67) and super-solar (Hyades) abundances bracketing NGC 6819’s composition. For the final temperature determination, we employ the photometry from Kalirai et al. (2001) since it possesses the highest precision in B and V photometry, as judged from the smaller scatter among their main sequence stars (see Figure 6). We find, and adopt, temperatures for the primary and secondary star of 6240 ± 80 K

and 5950 ± 70 K, respectively. These photometric temperatures are given in the last column of Table 2 and are consistent with the temperatures found spectroscopically (6350 ± 150 K; 5930 ± 150 K).

3.4. Binary-Star Modeling

Before computing binary star models, we removed some data points from consideration because of the possibility they could bias the results. Most importantly, we chose to restrict the photometric dataset to observations in and near the eclipses. Because the binary is well separated and not observed to vary significantly outside of eclipse, the out-of-eclipse observations contain little physical information on the binary. Variations in the photometry out of eclipse tended to make it more difficult to find the best fit to the eclipses (see Figure 4). Additionally, we shifted the V secondary-eclipse data from 2010 September 8 ($\phi = 0.46 - 0.52$) by $+0.062$ magnitudes. Initial light curves of 2010 September 8 showed the observations to be consistently fainter than Talamantes et al. (2010) observations over the same phase range. The observed difference is similar in amplitude to variations for rotating stars in young clusters (e.g. Meibom et al. 2011), but is smaller than the short-term variations ($\sim 0.01 - 0.02$ mag) seen in *Kepler* observations of this system. A smaller number of R_c observations were obtained on 2010 September 8, but no noticeable shift was evident in comparing to R_c observations on other nights. In the absence of a clear explanation, we opted to simply apply a zeropoint correction to the V data. We determined the shift by comparing out-of-eclipse observations from 2010 September 8 with those of 2008 June 5. Finally, we eliminated a handful of radial-velocity observations that were taken close to eclipse phases because they contributed disproportionately to the overall χ^2 of the fits and may have been affected by line blending. The eliminated points are shown as squares in Figure 5.

Models of the photometric and RV data were computed using the ELC code (Orosz & Hauschildt 2000). We employ ELC’s genetic and Markov optimizers to arrive at the best-fit solution. ELC employs the χ^2 statistic to describe the goodness-of-fit. The total χ^2 is the sum of individual χ^2 contributions from photometry for each filter, radial velocities for each component, and additional constraints derived from other observations. For WOCS 40007, our baseline model has eight free parameters: the inclination i ; velocity semi-amplitude of the primary K_1 ; temperature of the primary T_1 ; temperature ratio T_2/T_1 , ratio of the primary star radius to the semi-major axis \mathcal{R}_1/a ; ratio of the radii $\mathcal{R}_1/\mathcal{R}_2$; orbital period P ; and the time of primary eclipse minimum t_0 . To examine the effects of the limb-darkening treatment, we computed two kinds of models. First, we used a quadratic limb-darkening

law, assuming one coefficient for each star (from Claret 2000) and fitting for the other. This was done in the hope that an error in the assumed coefficient will be compensated for by a change in the value of the other because the coefficients are generally correlated (Southworth et al. 2007). Second, we employed PHOENIX model atmospheres (Hauschildt et al. 1997) to describe the variation of emitted intensity with emergent angle, which removes the need to assume limb-darkening coefficients. We include both limb-darkening and model atmosphere results in Table 4.

A cursory examination of the light and RV curves for WOCS 40007 reveals that there is little or no eccentricity. In test runs that allowed the eccentricity to vary, we found a best-fit solution with eccentricity $e = 0.0003 \pm 0.0001$ and argument of periastron passage $\omega = 90.0 \pm 0.1^\circ$. Therefore, we set the eccentricity to zero for all other model fits, which makes it possible to tightly constrain the orbit parameters K_1 and $q = \mathcal{M}_2/\mathcal{M}_1$ entirely using RV observations. We split the modeling into separate runs for the photometric and spectroscopic data. Eclipse timing variations from *Kepler* observations indicate the presence of a tertiary component (see §3.5), which meant that K_1 and q would be determined most precisely after the tertiary star orbit is fit and corrected for. Therefore, in our final fits of the photometry, we set the values of K_1 and q as observed constraints (described below).

Following the completion of the photometry model runs, we used the best-fit parameters (particularly i , P , and t_0) to determine the primary and secondary masses in a final RV model run. By completing the RV and photometric model optimization runs for WOCS 40007 separately, the relative weights of the RV and photometric measurements are not a concern, as they would be in a simultaneous fit to both.

To ensure that we derive realistic parameter uncertainties, we scale the error bars for our observations in order to obtain a reduced $\chi_\nu^2 = \chi_{\text{phot}}^2/\nu \approx 1$ (where ν is the number of degrees of freedom) for photometry in each filter and for the velocities measured for each star. Because the measurement uncertainties generally need to be scaled upward, this results in conservative uncertainties on the binary star model parameters because it allows a greater range of models to fit the data. The scatter around the best-fit model for the radial velocities gives an alternate estimate of the measurement uncertainty: 3.14 km s^{-1} for the primary star and 3.34 km s^{-1} for the secondary star. The scatter is significantly larger than the measurement precision for single stars (Hole et al. 2009, 0.4 km s^{-1} ;) due to spectral line blending, and with further correction to the RVs derived from our TODCOR analysis (see §3.2) is anticipated to decrease. The typical scaled uncertainty in each photometric observation is ~ 0.015 magnitudes for B , R_c , and I_c , and ~ 0.035 magnitudes for V . Uncertainties for each free and derived parameter were determined by projecting the n -dimensional χ^2 function onto each parameter. 1σ confidence intervals for the parameters are set where

the lower envelope of χ^2 values reaches $\chi_{min}^2 + 1$ (Avni 1976). Figure 7 shows the plots of parameter versus $\Delta\chi^2$.

Our best fit values for the free and derived parameters of the eclipsing binary can be seen in Table 4. The top portion of the table lists parameters that were fit during ELC runs, while the lower portion of the table lists parameters that were calculated from the values derived by ELC. For completeness, we include both model-atmosphere and limb-darkening results in the table. Both alternatives (use of model atmospheres or tabulated limb-darkening coefficients) will result in a degree of systematic error due to systematic errors in selecting the coefficients, or due to inappropriate vertical structure of the model atmospheres. Indeed, some parameters in Table 4 are not consistent within $1-\sigma$ uncertainties (e.g., \mathcal{R}_1 and \mathcal{R}_2). After some investigation, we found that this was because the atmosphere models were allowed to be nonspherical. When the limb darkening models were also allowed to be non-spherical, the best fit model agreed very well with the model atmosphere results. In spite of this, we adopt the tabulated limb-darkening results (with the assumption of sphericity) in later analyses. Our reason is that the derived radii can be sensitive to light curve shape near first and fourth contact, and star spots can affect the curves in these critical parts. If a spot is roughly centered on the side facing the other star, it can produce increasing brightness after the eclipse has completed, which is similar to the effects of nonsphericity. There is clear evidence of nonsynchronously rotating spots in *Kepler* light curves that can produce these effects, but no evidence of other out-of-eclipse light variations that would be associated with non sphericity.

Fits that are more constrained in this way understandably produce greater deviations between observations and model near eclipse ingress and egress, and therefore result in some disagreement in the radius-related parameters given in Table 4. By allowing some of the limb-darkening coefficients to be free parameters, we hope to minimize systematic errors in the radii of the stars.

Figures 3 and 4 show the ELC model over-plotted on our B , V , R_c , and I_c photometry and Figure 8 displays the $O - C$ diagrams for the four light curves. Our RV fit for WOCS 40007 is presented in Figure 5. Error bars are not shown in Figures 3 and 4 in order to clearly show the behavior of the observed light curve compared to the ELC model. Our photometric observations of WOCS 40007 clearly show that the secondary eclipse ($\phi = 0.5$) is total, allowing precise measurements of the radii of the primary and secondary components.

3.5. Detection of a Tertiary Star

As seen in Figure 6, WOCS 40007 is much redder than expected in the $(V, V - I_c)$ CMD. This hinted that a low-mass star could be blended with the eclipsing binary, though the presence of a third star has not been identified in the spectra. We have two sets of long-term measurements that could reveal such a star if it orbits the eclipsing binary: the center-of-mass velocities of the eclipsing binary monitored since 1998, and nearly continuous eclipse timing by the *Kepler* mission since 2009 and by earlier ground-based observers on a much more limited basis.

We did not attempt to model *Kepler* photometry here because it is difficult to be completely sure that instrumental trends are entirely removed, and that contamination from other stars is fully corrected for — this will be done in a later paper. As we are only interested in eclipse timing, we will not delve deeply into the reduction. The eclipses of WOCS 40007 are very clearly visible in the raw pixel data, although we did detrend the light curves for instrumental effects before determining eclipse timings using the method of Kwee & van Woerden (1956). We have also corrected for a 66.184 s error in the *Kepler* data, where times had been reported in UTC rather than TDB (barycentric dynamical time). Here we used long-cadence data from quarters 1-13 (excluding quarters 6 and 10 because the cluster fell on a dead CCD module), and the barycentric Julian dates (BJD) of middle eclipse typically had uncertainties of approximately 15 s. The eclipse timings are given in Table 5. For ground-based observations, the heliocentric Julian dates were converted to BJD using an online calculator⁵ (Eastman et al. 2010). Initially, the *Kepler* observations appeared to be consistent with a constant period, but by quarter 9 there was a noticeable deviation from a linear trend in the observed minus computed ($O - C$) diagram. A much earlier ground-based eclipse observation from Talamantes et al. (2010) also cannot be explained by a simple linear ephemeris. The gravitational influence of a third orbiting body can produce deviations from a linear ephemeris due to light travel time variations.

There would also be significant variations in the center-of-mass velocity of the binary introduced by a third body, so we did a simultaneous three-body fit to both the eclipse timings and the radial velocities of the primary and secondary stars, assuming that the third body is on a Keplerian orbit and interacting with the barycenter of the eclipsing binary. We therefore fit for the following parameters: the periods of the eclipsing binary P_b and tertiary P_3 ; the times of primary eclipse for the binary t_b and time of periastron for the tertiary t_3 (in BJD); and the eccentricity e_3 and argument of periastron ω_3 of the tertiary orbit (the eclipsing binary was assumed to be circular). These values are quoted in the top half of

⁵<http://astrutils.astronomy.ohio-state.edu/time/hjd2bjd.html>

Table 6. The largest effects on eclipse timing happen near periastron, which fortuitously occurred while *Kepler* has been observing. Our earliest eclipse timing (from ground-based observations in July 2001) appears to have occurred about the time of the previous periastron passage. This observation only phases with recent photometry if the binary period (in the absence of light travel time effects) is significantly smaller than is being observed now.

We computed radial velocities from the model, and compared with the observed radial velocities (see Figure 9). The reduced χ^2 values for the best unconstrained fit and the eclipse timing model are quite similar (0.99 vs. 1.19). The velocity semi-amplitudes of the binary components K_1 and K_2 , the binary barycenter K_b , and system velocity γ given in Table 6 were derived using the observed radial velocities and the eclipse timing model for the tertiary orbit. The radial velocities and eclipse timings both appear to have covered approximately one orbital period for the tertiary. We did not see evidence of an eclipse of the tertiary by either star in the binary in *Kepler* photometry to date, so the inclination of the tertiary orbit is undetermined. Future *Kepler* eclipse timing and ground-based radial velocities will help nail down the tertiary period and velocity amplitude. However, the solution of the tertiary orbit does not affect the measurements of the masses and radii of the eclipsing binary components significantly.

With the total mass of the eclipsing binary known (as discussed below), the velocity variation sets a lower limit for the mass of the tertiary. This would be the actual mass if the tertiary orbit has inclination $i = 90^\circ$. Using models of the radial velocities, we find that the minimum mass is about $0.56\mathcal{M}_\odot$.

Based on the lower limit to the tertiary mass, we can determine a faint limit for the tertiary star from stellar evolution models. We estimate the tertiary photometry by trying possible MS magnitudes between 19.0 and 20.5 in V . On the faint end, the tertiary properties are constrained by restricting the star to be on the cluster main sequence with a mass above the minimum derived above. On the bright end, the tertiary is constrained by its effects on the derived properties of the primary. The primary magnitude is dependent on the choice of the tertiary magnitude, while the secondary component remains at a fixed magnitude because its properties are determined from the secondary eclipse depth, which provides information on the combined primary and tertiary light (see Section 3.3). Selecting the best photometric match, we adopt a tertiary component with a B magnitude of 21.5 ± 0.4 , V magnitude of 20.1 ± 0.4 , R_c of 19.3 ± 0.4 , and I_c magnitude of 18.5 ± 0.4 .

The motion of the eclipsing binary induced by the tertiary has some small effects on the modeling of the binary star data, and these were noted earlier in §3.4. However, it should be noted that the period of the eclipsing binary P_b , the velocity semi-amplitudes K_1 and K_2 , and the mass ratio q given in Table 6 are the closest things to “true” — the values that

would be observed in the absence of the tertiary.

4. Photometric and Spectroscopic Results

4.1. Ephemeris for WOCS 40007

Because the gravity of the tertiary star causes shifts in the position of the eclipsing binary system relative to the observer, a linear ephemeris will be inadequate to predict eclipse timings to better than a few minutes. Readers should note that most of our ground-based observations were taken during times when the eclipsing binary was in a part of its orbit moving away from Earth with a nearly constant speed, and the extra light-travel time added during each orbit cycle resulted in a larger period measured at Earth (see Table 4). However, this is not the ephemeris that would be determined from observations while moving along with the binary. As stated earlier, our fit for the true orbital period of the eclipsing binary is given in Table 6.

4.2. Cluster Membership

Previous information about the membership of WOCS 40007 was rather limited. The system was too faint to be in the proper-motion study of Sanders (1972), and was identified by Hole et al. (2009) as a binary with unknown membership because its system velocity could not be reliably determined at the time. We are in a position now to discuss the binary’s membership using three different criteria.

First, based on its position 3′37 from the cluster center (1.4 core radii; Kalirai et al. 2001) and on the relative density of cluster and field stars at its magnitude level as estimated from Figure 3 of Kalirai et al., we determine a membership probability of 53%. This is the weakest constraint on membership though. Second, using the systemic velocity measured from our spectroscopic solution, we can calculate the membership probability using results of the radial-velocity survey of Hole et al. (2009):

$$p(v) = \frac{F_c(v)}{F_f(v) + F_c(v)}$$

where $F_c(v)$ and $F_f(v)$ are one-dimensional Gaussian functions describing the cluster and field RV distributions, respectively. We employed the Gaussian fit parameters given in Hole et al. (2009), and find that WOCS 40007 is a cluster member with a 84% probability.

The third membership measure involves proper-motion measurements (Platais et al., in preparation) combining old photographic plates with CCD observations using the 3.6 m Canada-France-Hawaii Telescope (CFHT). Although the star is isolated and optimally exposed on the images, there were somewhat larger than average astrometric errors in declination (0.27 mas y^{-1} , versus 0.14 mas y^{-1} in right ascension) likely due to coma present on the Hale 5 m telescope plates, which were the backbone of the astrometry. Despite this complication, we determine the astrometric membership probability to be 97%. As a result, we judge WOCS 40007 to be a cluster member.

4.3. Distance Modulus

The absolute magnitude and apparent distance modulus can be calculated using the radius from the binary star analysis and a temperature estimate. We calculated bolometric corrections in V from Vandenberg & Clem (2003), and used them along with the photometric temperature estimates to find $(m - M)_V = 12.49 \pm 0.10$ and 12.39 ± 0.11 for the two components of WOCS 40007. The distance moduli for the stars agree within the uncertainties, and the averaged distance modulus from the binary star components $[(m - M)_V = 12.44 \pm 0.07]$ is slightly larger than found from fits to older isochrone sets (12.35, Rosvick & Vandenberg 1998) or from the red clump analysis in §2.2. The largest contributor to the uncertainty in this distance modulus by far is the temperature. If we use the spectroscopic temperatures or the radii from the model atmosphere runs instead, the derived distance moduli only differ by about 0.03 mag and there is better consistency. However, with the other uncertainties that are present (e.g., the photometry of the primary star) this is not a clear reason to prefer one set of values over another.

5. Comparison with Stellar Evolution Isochrones

We use four different sets of theoretical stellar evolution isochrones to interpret the masses, radii and photometry of the WOCS 40007 stars. The four isochrone sets are: BaSTI (Pietrinferni et al. 2004), Dartmouth Stellar Evolution Program (DSEP; Dotter et al. 2008), Victoria-Regina (VR; Vandenberg et al. 2006) and Yonsei-Yale (Y^2 ; Demarque et al. 2004). We generate scaled-solar isochrones with parameters closest to the spectroscopic abundance for NGC 6819 ($[\text{Fe}/\text{H}] = +0.09$). Each model set differs from others in the physics inputs they employ, and these differences can result in systematic variations in the ages that are derived. As a result, it is worth identifying the factors that are most likely to affect the comparison between models and the stars in the WOCS 40007 binary and those that will affect the

overall CMD comparison.

For example, convective core overshoot (CCO) is believed to occur for stars with $\mathcal{M} \gtrsim 1.1 \mathcal{M}_\odot$ (the exact value depends on the input chemical composition; Gallart et al. 2005), and so it is expected to be acting in the primary star of WOCS 40007 and possibly also the secondary star. However, the effects of CCO are not clearly identifiable until a star is near the cluster turnoff when CCO can mean the difference between continued core fusion and central hydrogen exhaustion. That translates into a large structural (radius) difference between models that have different degrees of CCO. Thus CCO will primarily affect comparisons in the CMD near the cluster turnoff.

CCO is handled in similar ways for all isochrone sets except for VR. VR isochrones use a parameterized version of the Roxburgh criterion (see Roxburgh 1989; Rosvick & Vandenberg 1998) and integrates fluid dynamics equations using observationally determined parameters to constrain the amount of CCO present. BaSTI, DSEP, and Y² force the amount of CCO to increase as the stellar mass increases, using

$$\lambda_{OV} = \Lambda_{OS} H_p$$

where λ_{OV} is the distance convective cells travel beyond the edge of the convective zone as defined by the Schwarzschild criterion, Λ_{OS} is a characteristic CCO parameter, and H_p is the local pressure scale height. The precise shape of the isochrone is affected by how Λ_{OS} varies as a function of stellar mass. We refer the reader to the original papers for a full description of the CCO algorithm adopted by each isochrone set. However, to get an idea how this might influence the models, we compare below the amount of CCO used in each of the isochrone sets for stars with masses at the cluster turnoff of NGC 6819 (Sandquist et al. 2013, $\sim 1.47 \mathcal{M}_\odot$) or like those stars in the WOCS 40007 binary (1.24 and $1.09 \mathcal{M}_\odot$).

In the BaSTI isochrones (Pietrinferni et al. 2004), Λ_{OS} is dependent on mass but not on metallicity, and generally lower than for the other isochrone sets: 0.14 at the turnoff, and 0.09 and 0.05 for the binary star masses. For Y² isochrones (Demarque et al. 2004), $\Lambda_{OS} = 0$ and 0.05, respectively, for the components of WOCS 40007 because the onset of CCO is triggered at a relatively high mass in those models. However, Λ_{OS} has reached its maximum value (0.20) for the turnoff of the cluster. DSEP parameterizes CCO by adopting the same Λ_{OS} treatment as Y², and the values for the WOCS 40007 components and the cluster turnoff appear to be the same. It should be remembered, however, that some CCO may be the result of rotationally induced mixing, which is not taken into account by any of these models.

The rate of the $^{14}\text{N}(p, \gamma)^{15}\text{O}$ nuclear reaction rate is important because it sets both the strength of the CNO cycle and the extent of the convective core, and it has seen significant

revision in recent years (Marta et al. 2008). Current public isochrone sets generally use older and larger values for the rate. The exception is DSEP, which uses an earlier rate coefficient (Imbriani et al. 2004) that is close to the most recent value. This would tend to reduce the extent of core convection in the DSEP isochrones relative to other sets. Helium diffusion (which is only employed in DSEP and Y^2 isochrones) can also potentially have an effect on the rate at which helium builds up in the cores of stars.

Although the two eclipsing stars in WOCS 40007 have evolved significantly in radius compared to zero-age stars, they are still on the main sequence somewhat below the cluster turnoff and their characteristics will not be as sensitive to age as stars nearer the turnoff (such as WOCS 23009; Sandquist et al. 2013).

5.1. Age of NGC 6819

5.1.1. CMD Comparison

As a first check, we investigate how each isochrone set matches the CMD of NGC 6819 in the traditional way, using the reddening and distance determined in Section 2.2. In Figure 10, we plot the CMD with probable single-star cluster members brighter than the $V \sim 16.5$ magnitude limit of the WOCS RV survey (Hole et al. 2009). Below this magnitude limit, we plot all measured stars in $B - V$ (data from Kalirai et al. 2001) and $V - I_c$ (Talamantes et al. 2010). The presence of CCO in stars near the turnoff of NGC 6819 is suggested by the cluster members near $(B - V, V) = (0.6, 14.6)$.

The BaSTI isochrones were generated using a metallicity $[\text{Fe}/\text{H}] = +0.06$, which was the tabulated value closest to the spectroscopic measurement for NGC 6819. The theoretical MS is slightly redder than the cluster main sequence in the $(B - V)$ CMD, but the isochrones agree reasonably well with the CCO-sensitive stars of the blue hook at the turnoff. DSEP isochrones, made with $[\text{Fe}/\text{H}] = +0.09$, produce the best overall fit to the CMD, and the MS of the isochrones and CMD are well aligned.

VR isochrones were created with $[\text{Fe}/\text{H}] = +0.13$, which again was the tabulated value closest to the spectroscopic measurement. This isochrone set produces a giant branch that is slightly too blue and misses a majority of the MS by being too red, likely in part because the isochrone metallicity is larger than the spectroscopic value for the cluster. In the vicinity of the turnoff, the isochrones are generally too bright and/or red. In the Y^2 models, the giant branch is again slightly too blue in $(B - V)$, but the MS fits well. photometry in $(B - V)$. Strangely, the isochrones show much worse agreement on the main sequence and at the turnoff in $(V - I)$.

Given that there is uncertainty in the distance and reddening for the cluster, we examine a second way of using isochrones by aligning them in the CMD with the binary components at the observed mass values. We use the $B - V$ decomposition of WOCS 40007 from the Kalirai et al. (2001) photometry because it had the highest signal-to-noise ratio for MS stars in the photometric datasets. Because the photometry of the secondary component is independent of assumptions about the tertiary star, we choose to force the isochrones to match the secondary star’s mass, V magnitude, and $B - V$ color. With this alignment, the primary component lies within the range predicted by the isochrones, although in some cases it lies near the lower photometric limit (see Figure 11).

With this type of fit, age information comes exclusively from the photometry of cluster stars at the main sequence turnoff. Given that the components of WOCS 40007 fall near the blue edge of the main sequence, a good isochrone fit should follow that edge. BaSTI isochrones do a decent job predicting the location of the giant branch, but fail to properly fit the turnoff and subgiant branch simultaneously. The 2.0 Gyr isochrone displays the best fit to the turnoff, but has a subgiant branch that is too bright. As mentioned earlier, this disagreement is probably the result of the smaller amount of CCO used in these models. DSEP isochrones fit well throughout the main sequence, turnoff, subgiant branch, and red giant branch for an age of 2.5 Gyr. For the VR isochrones, the turnoff is fit for an age of about 2.3 Gyr, but the subgiant branch is again too bright. Lastly, the Y^2 isochrones align well with the giant branch and the turnoff, leading to a best fit age of slightly below 2.5 Gyr. Table 7 lists the best fit age for each isochrone in the “CMD Isochrone” column.

When fitting the isochrone to the binary components, there is an implied reddening and distance modulus. The distance derived from the fit to the secondary star agrees with our determination from the binary star components in Section 4.3 ($(m - M)_V = 12.44 \pm 0.07$) to within about 1σ for the BaSTI [$(m - M)_V = 12.35$], DSEP (12.40), and VR (12.36) isochrone sets, while the Y^2 value (12.28) differs by slightly more than 2σ . There is additional uncertainty in values derived by fitting to the primary star due to poor constraints on the properties of the tertiary star, and generally the distance moduli are larger (12.45, 12.51, 12.41, and 12.39 for BaSTI, DSEP, VR, and Y^2 , respectively). The difference is most likely a result of uncertainties in the photometric decomposition, but additional effort to detect and characterize the tertiary star would settle the question.

5.1.2. Ages from the Mass-Radius Plane

We compare the measured masses and radii of the known bright binary components with model predictions. Ultimately we wish to use all of measurable cluster stars for an analysis

of the cluster age using this technique. For the analysis below, we are including the primary star of the WOCS 23009 system (Sandquist et al. 2013), although it should be remembered that WOCS 23009 is a single-lined spectroscopic binary. As such, the primary star’s mass had to be estimated using the masses and V magnitudes of WOCS 40007 in concert with theoretical models. Because the estimated mass for that star varied from model to model due to differences in the adopted physics, the position of the error box varies slightly in these diagrams.

$M - R$ diagrams for each isochrone set are shown in Figure 12. The error boxes for the components of WOCS 40007 correspond to 1σ uncertainties determined in §3.4. The radius uncertainties are relatively small because the secondary eclipse is total. Thus, it is the precision of the mass measurements that currently determines the attainable age precision, and the mass precision could be improved with additional, more precise radial velocity measurements and an improved determination of the tertiary star orbit. Table 7 shows the ages that we derive from the respective $M - R$ isochrone fits from Figure 12. The ages derived from BaSTI, DSEP, and VR models using only the components of WOCS 40007 agree very well, while the Y^2 age is systematically higher.

The characteristics of the primary star indicate an age of 2.9 – 3.3 Gyr from different isochrones with fitting uncertainties of 0.5 Gyr, while the secondary returns 3.3–3.7 Gyr with fitting uncertainties of 0.8 Gyr. The age determined from the secondary star is systematically higher, but there is a range of isochrones that give a consistent age for both components within the present 1σ mass uncertainties. Both stars of WOCS 40007 imply greater ages than the more massive primary star of WOCS 23009, but the two systems have consistent ages within 2σ . If we take the measurements at face value though, the $M - R$ diagram analysis of WOCS 40007 produces a weighted average age estimate of 3.1 ± 0.4 Gyr, where the statistical uncertainty is given. If the primary star of WOCS 23009 is included in the weighted average, the age estimate shifted significantly downward to 2.5 ± 0.2 Gyr. In both cases, there is a systematic uncertainty of at least 0.2 Gyr resulting from model uncertainties.

Based on evidence from field binary stars, there are reasons to believe that the stars of WOCS 40007 could have somewhat anomalous radii. Secondary stars of similar mass ($0.80 - 1.10\mathcal{M}_\odot$) in field eclipsing binaries with smaller periods (0.6 – 2.8 d) typically possess radii that are larger than predictions and temperatures that are cooler (Clausen et al. 2009). The cause is thought to be rotation-driven magnetic activity that inhibits convective energy transport in the outer layers. WOCS 40007 has a period just outside this interesting range, and magnetic activity would probably affect the secondary to a greater degree due to its more massive convective envelope. The primary component of WOCS 23009 is in a *much* longer period binary and is likely to have an even smaller convective envelope, so that it is unlikely

to be affected by stellar activity. Regardless of the presence of magnetic activity, rotation in MS and turnoff stars may cause an apparent shift of the stars in the CMD (Girardi et al. 2011), but if the star in WOCS 23009 have synchronized rotation, the rotation is probably too small to be a significant effect. A recent study by Kaluzny et al. (2013) on the globular cluster M4 found that different stars yield somewhat different ages and that the secondary stars yielded larger age estimates, although at a statistically significant level. To more strongly test whether all three stars are consistent with a single age or whether one or both of the stars in WOCS 40007 are significantly inflated, we will need more precise radial-velocity measurements in order to reduce the mass uncertainties.

The age estimate found from the analysis of the CMD in this and previous studies of the cluster (Kalirai et al. 2001; Rosvick & Vandenberg 1998) agrees best with the age estimates from the primary component of WOCS 23009. While this may be an indication that the stars in WOCS 40007 are inflated in size, isochrones in the $M - R$ diagram shift significantly with chemical composition. Therefore, we should consider the possibility that the adopted metallicity may be incorrect or that another composition variable (like helium; Brogaard et al. 2011) may differ from what is assumed in the models. We tested this idea by changing the assumed $[\text{Fe}/\text{H}]$ by 0.1 dex, which is significantly larger than the statistical uncertainty in the cluster metallicity reported by Bragaglia et al. (2001), but within the range of possibilities for typical systematic scale errors in abundance studies. Figure 13 displays isochrones in the $M - R$ plane with a metallicity decreased by 0.1 dex (which would make it closer in composition to M67), and Figure 14 shows the same lower metallicity isochrones in the CMD. We find that a decreased metallicity produces slightly greater consistency between the ages implied by the two stars in WOCS 40007. Additionally, the lower metallicity produces ages are lower (by about 0.2 Gyr) from the stellar masses and radii, and those ages are more consistent with those derived from CMD fits. The comparison of lower metallicity isochrones with the CMD returns ages of $\sim 2.25 - 2.50$ Gyr for the DSEP, VR, and Y^2 sets. (BaSTI is not considered here because the tabulated isochrones with metallicity nearest to the reduced value is -0.25 , which is well below the prescribed 0.1 dex.) In each case, the age is more consistent with previously reported ages of the cluster. The cluster turnoff is fit reasonably well by the lower metallicity isochrones, although this is also influenced by the convective overshooting prescription. Future spectroscopic work should be able to leverage the precise gravities from the binary stars to improve the abundance analysis for stars at the cluster turnoff and further investigate this possibility (Brogaard et al. 2011).

6. Summary & Conclusions

We have presented an extensive photometric and RV study of the detached eclipsing binary star WOCS 40007 in NGC 6819 as part of a larger project to precisely determine the age of the cluster. We use our precision mass and radius determination measurements (uncertainties of $\sim 1.6\%$ and 0.5% , respectively) to derive an age of NGC 6819 of 3.1 ± 0.4 Gyr using BaSTI, DSEP, and VR isochrones, while the best fit age for Y^2 isochrones is slightly larger. The primary star of the brighter (and longer period) binary WOCS 23009 indicates an age closer to 2.5 Gyr, which is more consistent with the results from fitting isochrones in the CMD. However, the age results are consistent to within $1 - 2\sigma$ uncertainties.

The $M - R$ comparison is unaffected by many of the systematic uncertainties that affect other methods of age determination (e.g., CMD isochrone fitting), but is affected by chemical composition uncertainties. The uncertainty in the age estimate from the measured eclipsing stars is currently dominated by the uncertainties in the stellar masses and the cluster chemical composition. There is an indication that a slightly smaller metallicity would produce greater consistency between mass-radius and CMD results. The possibility of a lower cluster metallicity can still be spectroscopically tested using the binary stars with the assistance of constraints on the surface gravities from the binary-star analysis. In addition, more precise mass measurements will help test whether the radii of the WOCS 40007 stars are systematically high due as a consequence of their relatively short orbital period.

With further work on known DEBs and forthcoming DEB discoveries in NGC 6819 from *Kepler*, the age constraints from the $M - R$ diagram will be significantly tightened. An increased population of stars with well-determined mass, radius and photometric properties will strongly constrain the fits in both the $M - R$ diagram and the CMD, producing a situation where the input physics of the isochrones may be thoroughly tested.

We would like to thank the Director of Mount Laguna Observatory (P. Etzel) for generous allocations of observing time and A. Talamantes for his time and effort on observing and reducing a majority of the V -band images at the MLO 1-meter. Many thanks to E. Bavarsad and D. Baer for their assistance with the observations at MLO.

This paper includes data collected by the *Kepler* mission. Funding for the *Kepler* mission is provided by the NASA Science Mission directorate. We are grateful to the *Kepler* team for the opportunity to work with such a precise and extensive photometric dataset. We gratefully acknowledge funding from the National Science Foundation under grant AST-0908536 to San Diego State University and AST-0908082 to the University of Wisconsin-Madison, and from the National Aeronautics and Space Administration (NASA) under grant G00008957. KB

acknowledges funding from the Carlsberg Foundation and the Villum Foundation.

REFERENCES

- Alard, C. 2000, *A&AS*, 144, 363
- Andersen, J. 1991, *A&A Rev.*, 3, 91
- Auner, G. 1974, *A&AS*, 13, 143
- Avni, Y. 1976, *ApJ*, 210, 642
- Basu, S. et al. 2011, *ApJ*, 729, L10
- Blackwell, D. E., Petford, A. D., & Shallis, M. J. 1980, *A&A*, 82, 249
- Bragaglia, A. et al. 2001, *ApJ*, 121, 327
- Bragaglia, A. 2008, *Mem. Soc. Astron. Italiana*, 79, 365
- Brogaard, K., Bruntt, H., Grundahl, F., Clausen, J. V., Frandsen, S., Vandenberg, D. A., & Bedin, L.R. 2011, *A&A*, 525, 2
- Brogaard, K., Vandenberg, D. A., Bruntt, H., et al. 2012, *A&A*, 543, A106
- Burkhead, M. S. 1971, *AJ*, 76, 251
- Canterna, R., Geisler, D., Harris, H. C., Olszewski, E., & Schommer, R. 1986, *AJ*, 92, 1
- Casagrande, L., Ramírez, I., Meléndez, M., & Asplund, M. 2010, *A&A*, 512, A54
- Castelli, F., & Kurucz, R. L. 2003, *Modelling of Stellar Atmospheres*, 210, 20P
- Castelli, F., & Kurucz, R. L. 2004, [arXiv:astro-ph/0405087](https://arxiv.org/abs/astro-ph/0405087)
- Claret, A. 2000, *A&A*, 363, 1081
- Clausen, J. V., Baraffe, I., Claret, A., & Vandenberg D. A. 1999, in *Theory and Tests of Convection in Stellar Structure*, ed. A. Giménez, E. F. Guinan, & B. Montesinos, *ASP Conf. Ser.*, 173, 265
- Clausen, J. V. et al. 2009, *A&A*502, 253
- Clausen, J. V., Olsen, E. H., Helt, B. E., & Claret, A. 2010, *A&A*, 516, 42

- Corsaro, E., Stello, D., Huber, D., et al. 2012, *ApJ*, 757, 190
- Demarque, P., Woo, J. H., Kim, Y. C., & Yi, S. K. 2004, *ApJS*, 155, 667
- Dotter, A. et al. 2008, *ApJS*, 178, 89
- Eastman, J., Siverd, R., & Gaudi, B. S. 2010, *PASP*, 122, 935
- Friel, E. D., Liu, T., & Janes, K. A. 1989, *PASP*, 101, 1105
- Friel, E. D., & Janes, K. A. 1993 *A&A*, 267, 75
- Gallart, C., Zoccali, M., & Aparicio, A. 2005, *ARA&A*, 43, 387
- Geller, A. G., Mathieu, R. D., Harris, H. C., & McClure, R. D. 2008, *AJ*, 135, 2264
- Girardi, L., & Salaris, M. 2001, *MNRAS*, 323, 109
- Girardi, L., Eggenberger, P., & Miglio, A. 2011, *MNRAS*, 412L,103G
- Grocholski, A. J., & Sarajedini, A. 2002, *AJ*, 123, 1603
- Grundahl, F., Clausen, J. V., Hardis, S., & Frandsen, S. 2008, *A&A*, 492, 171
- Hauschildt, P. H., Baron, E., & Allard, F. 1997, *ApJ*, 483, 390
- Hole, K. T., Geller, A. M., Mathieu, R. D., Platais, I., Meibom, S., & Latham, D. W. 2009, *AJ*, 138, 159
- Imbriani, G., Costantini, H., Formicola, A., et al. 2004, *A&A*, 420, 625
- Kalirai, J. S. et al. 2001, *AJ*, 122, 266
- Kalirai, J.S. & Tosi, M. 2004, *MNRAS*, 351, 649
- Kaluzny, J. et al 2013, *AJ*, 145, 43K
- Kang, Y.-W., & Ann, H.B. 2002, *J. Korean Astron. Soc.*, 35, 87
- Kwee, K.K, & van Woerden, H. 1956, *Bull. Astron. Inst. Netherlands*, 12, 327
- Latham, D. W. et al. 2002, *AJ*, 124, 1144
- Lindoff, U. 1972, *A&AS*, 7, 497
- Marta, M., Formicola, A., Gyürky, G., et al. 2008, *Phys. Rev. C*, 78, 022802

- Mathieu, R. D. 2000, ASP, 198, 517
- McCall, M. L. 2004, AJ, 128, 2144
- Meibom, S. et al. 2009, AJ, 137, 5086
- Meibom, S., Mathieu, R. D., Stassun, K. G., Liebesny, P., & Saar, S. H. 2011, ApJ, 733, 115
- Milliman, K. E., et al. 2013, AJ, in preparation
- Orosz, J. A., & Hauschildt, P. H. 2000, A&A, 364, 265
- Pietrinferni, A., Cassisi, S., Salaris, M., & Castelli, F. 2004, AJ, 612, 168
- Popper, D. M., Lacy, C. H., Frueh, M. L., & Turner, A. E. 1986, AJ, 91, 383
- Popper, D. M., 1997, AJ, 114, 1195
- Prša, A., et al. 2011, AJ, 141, 83
- Roxburgh, I. W. 1989, A&A, 211, 361
- Rosvick, J. M., & Vandenberg, D. A. 1998, AJ, 115, 1516
- Sanders, W. L. 1972, A&A, 19, 155
- Sandquist, E. L. 2004, MNRAS, 347, 101
- Sandquist, E. L., Mathieu, R. D., Brogaard, K., et al. 2013, ApJ, 762, 58
- Sandquist, E. L., Serio, A. W., & Shetrone, M. 2011, AJ, 142, 194
- Skrutskie, M. F., Cutri, R. M., Stiening, R., et al. 2006, AJ, 131, 1163
- Slawson, R. W., Prša, A., Welsh, W. F., et al. 2011, AJ, 142, 160
- Southworth, J., Bruntt, H., & Buzasi, D. L. 2007, A&A, 467, 1215
- Stetson, P. B. 1987, PASP, 99, 191
- Stetson, P. B. 1990, PASP, 102, 932
- Talamantes, A., Sandquist, E. L., Clem, J. L., Robb, R. M., Balam, D. D., & Shetrone, M. 2010, AJ, 140, 1268
- Taylor, B. J. 2007, AJ, 133, 370

- Torres, G., Andersen, J., & Giménez, A. 2010, *A&A Rev.*, 18, 67
- Twarog, B. A., Ashman, K., & Anthony-Twarog, B. 1997, *AJ*, 114, 2556
- VandenBerg, D. A., Bergbusch, P. A., & Dowler, P. D. 2006, *ApJS*, 162, 375
- VandenBerg, D. A., Casagrande, L., & Stetson, P. B. 2010, *AJ*, 140, 1020
- VandenBerg, D. A., & Clem, J. L. 2003, *AJ*, 126, 778
- Zucker, S., & Mazeh, T. 1994, *ApJ*, 420, 806

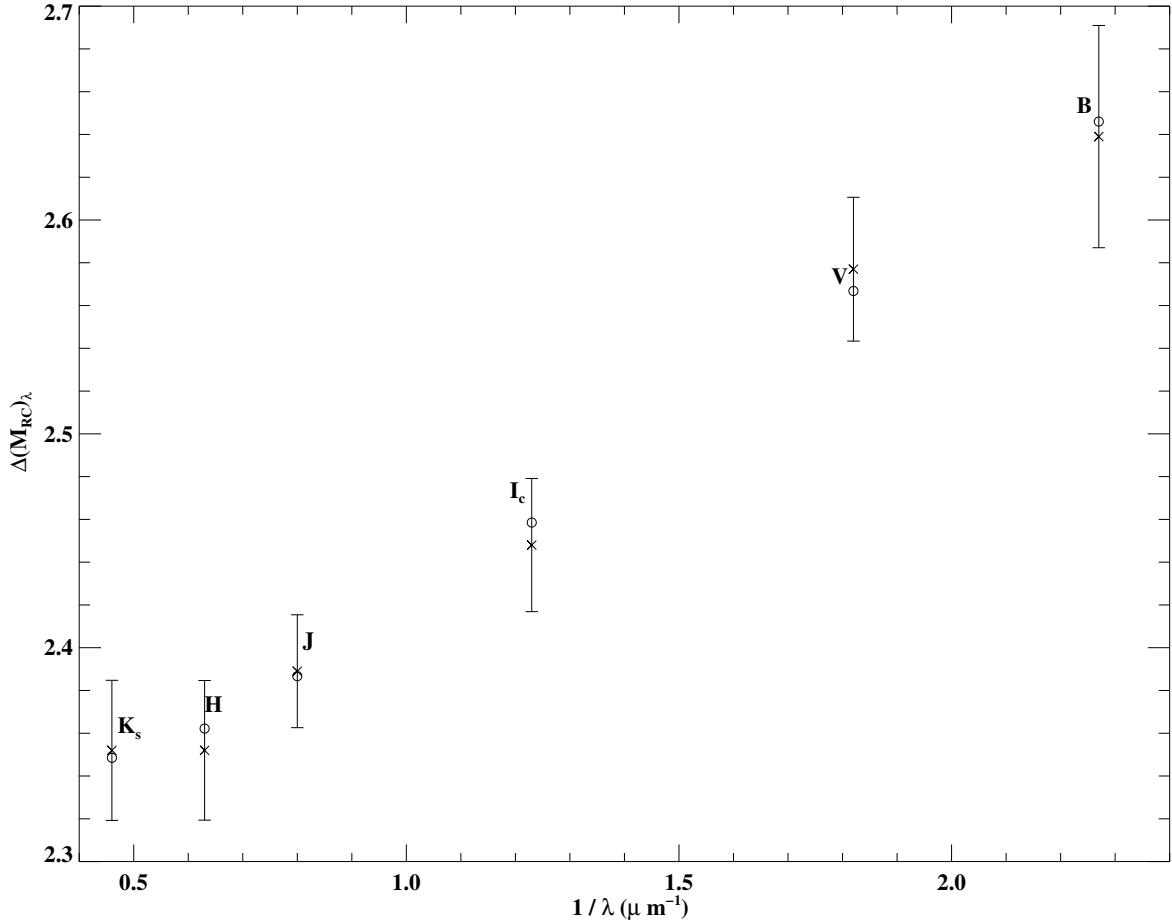


Fig. 1.— The difference in median clump magnitude in B , V , I_c , J , H , and K_s , as a function of wave number ($1/\lambda$) between NGC 6819 and M 67. Crosses show measured values, while open circles indicate the best fit using the extinction algorithm of McCall (2004).

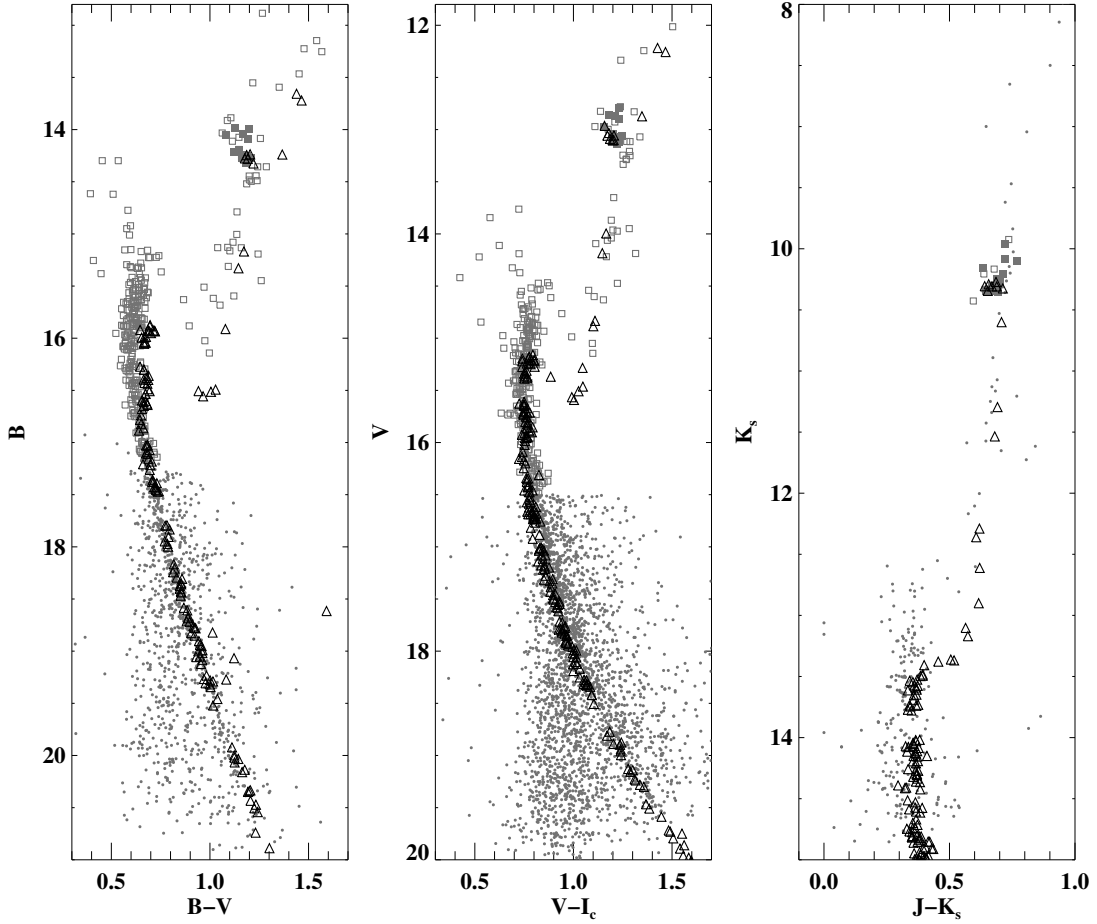


Fig. 2.— Comparison of CMDs of M67 and NGC 6819. Single-star members of M67 (Sandquist 2004) are plotted as open triangles. M67 stars have been shifted in B , V and K_s magnitude by 2.646, 2.567, and 2.349, respectively. Color shifts of $\Delta(B - V) = 0.079$, $\Delta(V - I_c) = 0.108$, and $\Delta(J - K_s) = 0.038$ mag are also applied. Open grey squares represent single-star members of NGC 6819 and the filled grey squares are the known red clump population (Hole et al. 2009). Grey dots with $V > 16.5$ are from the full CMD of Talamantes et al. (2010).

Table 1. Photometric Observations at Mount Laguna Observatory 1-meter

Date	Filters	mJD ^a Start	t_{exp} (s)	N
2010 Jun. 14	<i>B</i>	5362.725	600	31
2010 Jun. 22	<i>B</i>	5370.708	600	37
2010 Jun. 23	<i>B</i>	5371.687	600	38
2010 Jun. 25	<i>V</i>	5373.680	600	34
2010 Jul. 08	<i>I_c</i>	5386.680	300	95
2010 Jul. 19	<i>I_c</i>	5397.664	300	100
2010 Jul. 21	<i>B</i>	5399.662	600	45
2010 Aug. 20	<i>R_c</i>	5429.649	420	60
2010 Aug. 28	<i>V</i>	5437.649	600	36
2010 Aug. 31	<i>R_cI_c</i>	5440.626	420, 300	36, 22
2010 Sep. 01	<i>B</i>	5441.824	600	13
2010 Sep. 08	<i>VR_c</i>	5448.618	600, 420	19, 16
2010 Sep. 14 ^b	<i>BVR_c</i>	5454.780	600, 600, 480	7, 1, 7
2010 Sep. 17 ^b	<i>VR_cI_c</i>	5457.733	600, 480, 300	10, 10, 10
2010 Sep. 21 ^b	<i>BVR_c</i>	5461.770	600, 600, 480	5, 5, 5
2010 Sep. 22 ^b	<i>BVR_cI_c</i>	5462.604	600, 600, 480, 300	8, 8, 13, 17
2010 Oct. 02 ^b	<i>BVR_cI_c</i>	5472.596	600, 600, 480, 300	4, 2, 5, 6
2010 Oct. 11 ^b	<i>BVR_cI_c</i>	5481.584	600, 600, 480, 300	8, 9, 7, 12
2010 Oct. 17 ^b	<i>VR_cI_c</i>	5487.583	600, 480, 300	6, 9, 10
2010 Oct. 30 ^b	<i>VR_cI_c</i>	5500.598	600, 480, 300	8, 8, 12
2010 Nov. 03	<i>R_cI_c</i>	5504.581	480, 300	19, 16
2010 Nov. 12	<i>I_c</i>	5513.560	300	41
2011 May 22	<i>BV</i>	5704.801	600, 600	6, 14
2011 Jun. 02	<i>BV</i>	5715.738	600, 600	11, 13
2011 Jun. 06	<i>VI_c</i>	5719.722	600, 300	14, 14
2011 Jun. 11	<i>V</i>	5724.725	600	36
2011 Jul. 03	<i>I_c</i>	5746.663	300	12
2011 Jul. 14	<i>R_c</i>	5757.660	300	62
2011 Jul. 23	<i>I_c</i>	5766.657	300	83
2011 Jul. 25	<i>BI_c</i>	5768.661	600, 300	36, 41
2011 Aug. 14	<i>I_c</i>	5788.643	300	64

Table 1—Continued

Date	Filters	mJD ^a Start	t_{exp} (s)	N
2011 Aug. 25	<i>BV</i>	5799.634	600, 600	17, 18
2011 Sep. 16	<i>BV</i>	5821.637	600, 600	17, 15

^amJD = HJD - 2 450 000

^bBoth twilight and dome flat fields used in the *IRAF* reduction.

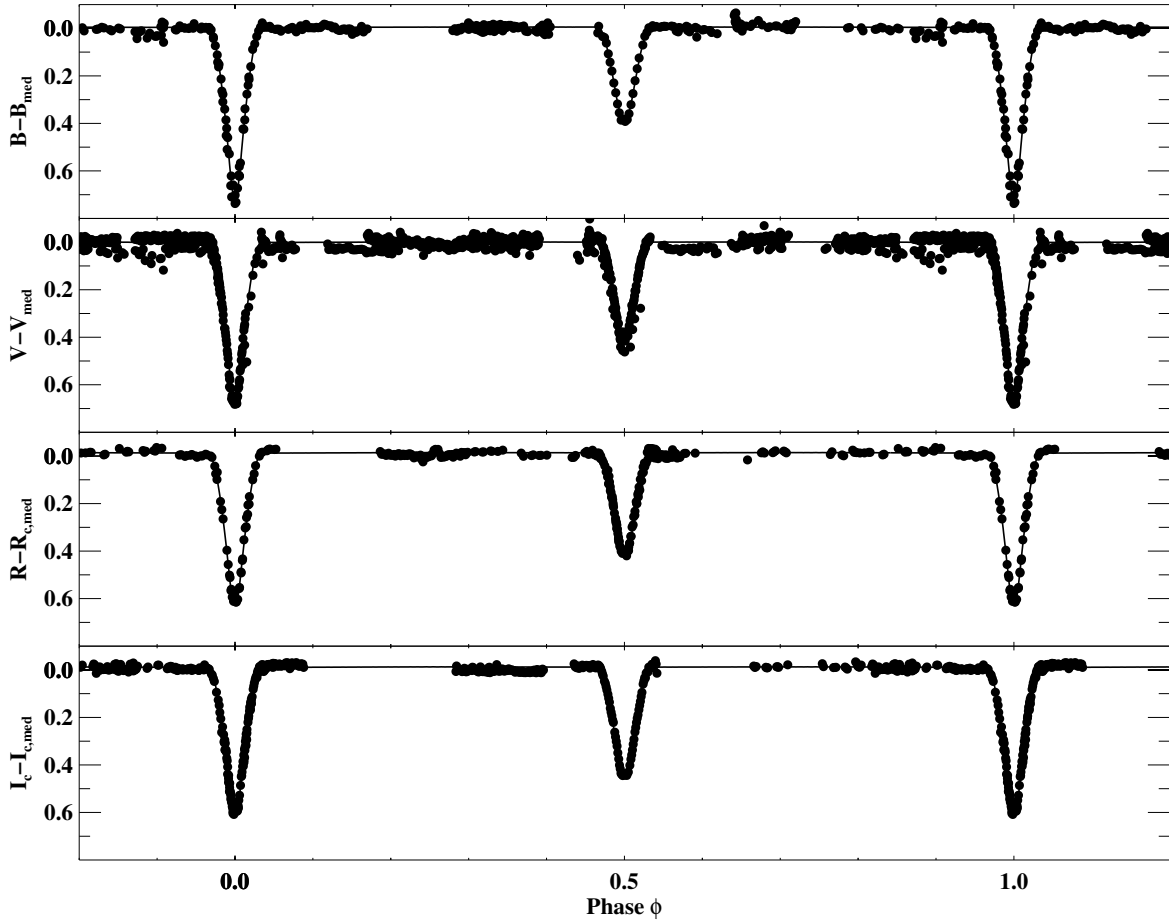


Fig. 3.— Photometry for WOCS 40007, phased to the orbit period for each filter. The solid line is the ELC model fit.

Table 2. Standard-system DEB Magnitudes and Effective Temperatures

Name	B	V	R_c	I_c	T_{eff} (K) ^a
WOCS 40007	16.356 ± 0.016	15.651 ± 0.016		14.774 ± 0.018	
WOCS 40007 _p	16.739 ± 0.017	16.072 ± 0.017		15.231 ± 0.019	
WOCS 40007 _s	17.650 ± 0.019	16.896 ± 0.019		15.944 ± 0.021	
WOCS 40007 ₃	21.2 ± 0.4	19.8 ± 0.4		18.3 ± 0.4	
Δm_s ^b	0.393 ± 0.046	0.415 ± 0.024	0.402 ± 0.032	0.452 ± 0.032	
Rosvick & Vandenberg (1998)					
WOCS 40007 ^c	16.287 ± 0.015	15.622 ± 0.010		14.770 ± 0.019	
WOCS 40007 _p	16.698 ± 0.093	16.072 ± 0.039		15.291 ± 0.068	
WOCS 40007 _s	17.581 ± 0.214	16.867 ± 0.080		15.940 ± 0.124	
Kalirai et al. (2001)					
WOCS 40007 ^c	16.299	15.633			
WOCS 40007 _p	16.705	16.074			6240 ± 80
WOCS 40007 _s	17.593	16.878			5950 ± 70
Hole et al. (2009) — Phot03					
WOCS 40007 ^c	16.294	15.631			
WOCS 40007 _p	16.705	16.081			
WOCS 40007 _s	17.588	16.876			
Hole et al. (2009) — Phot98					
WOCS 40007 ^c	16.311	15.657	15.247^{d}	14.824	
WOCS 40007 _p	16.722	16.108	15.874	15.349	
WOCS 40007 _s	17.605	16.902	16.521	15.994	

^aTemperature scale of Casagrande et al. (2010). See Section 3.3 for a complete discussion.

^b Δm_s is the secondary eclipse depth relative to phases immediately before or after eclipse.

^cCalibrated system photometry has been shifted to the photometric zeropoints of this study.

^dHole et al. (2009) R_c photometry has not been shifted to our photometric zeropoints.

Table 3. Comparison of Photometric Zeropoints Relative to Talamantes et al. (2010)

Source	ΔB	ΔV	ΔI_c	$\Delta(B - V)$	$\Delta(V - I_c)$
Rosvick & Vandenberg (1998)	-0.026 (0.042)	-0.015 (0.033)	-0.066 (0.032)	-0.011 (0.023)	0.049 (0.020)
Kalirai et al. (2001)	-0.046 (0.033)	-0.042 (0.029)		-0.001 (0.018)	
Hole et al. (2009) Phot03	-0.026 (0.021)	-0.019 (0.017)		-0.004 (0.012)	
Hole et al. (2009) Phot98	-0.004 (0.025)	-0.001 (0.027)	-0.013 (0.027)	+0.002 (0.018)	+0.019 (0.022)

Note. — Quoted values are for the median difference, with the semi-interquartile range in parentheses.

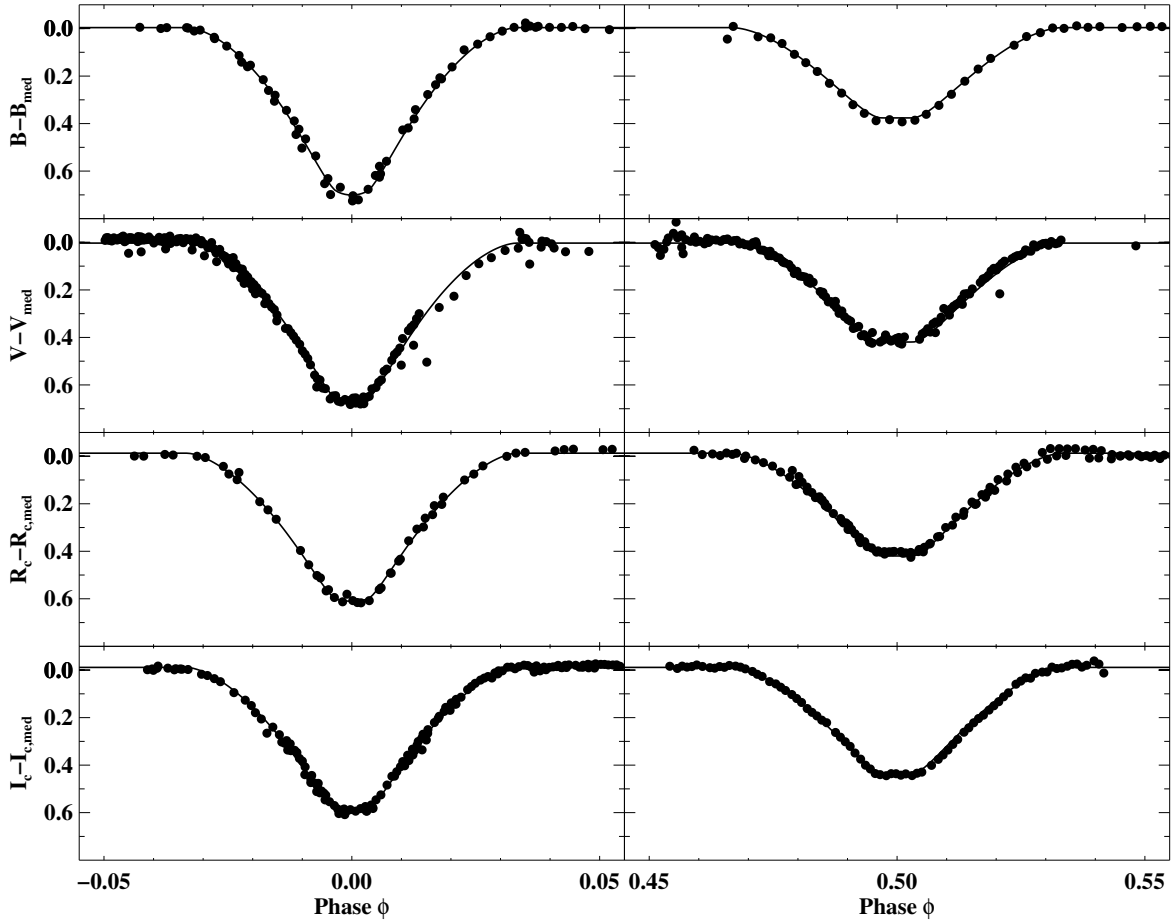


Fig. 4.— Photometry for WOCS 40007, zoomed in on the primary (left column) and secondary (right column) eclipses. The black line corresponds to the ELC model fit. This restricted set of data was used to determine the best fit model.

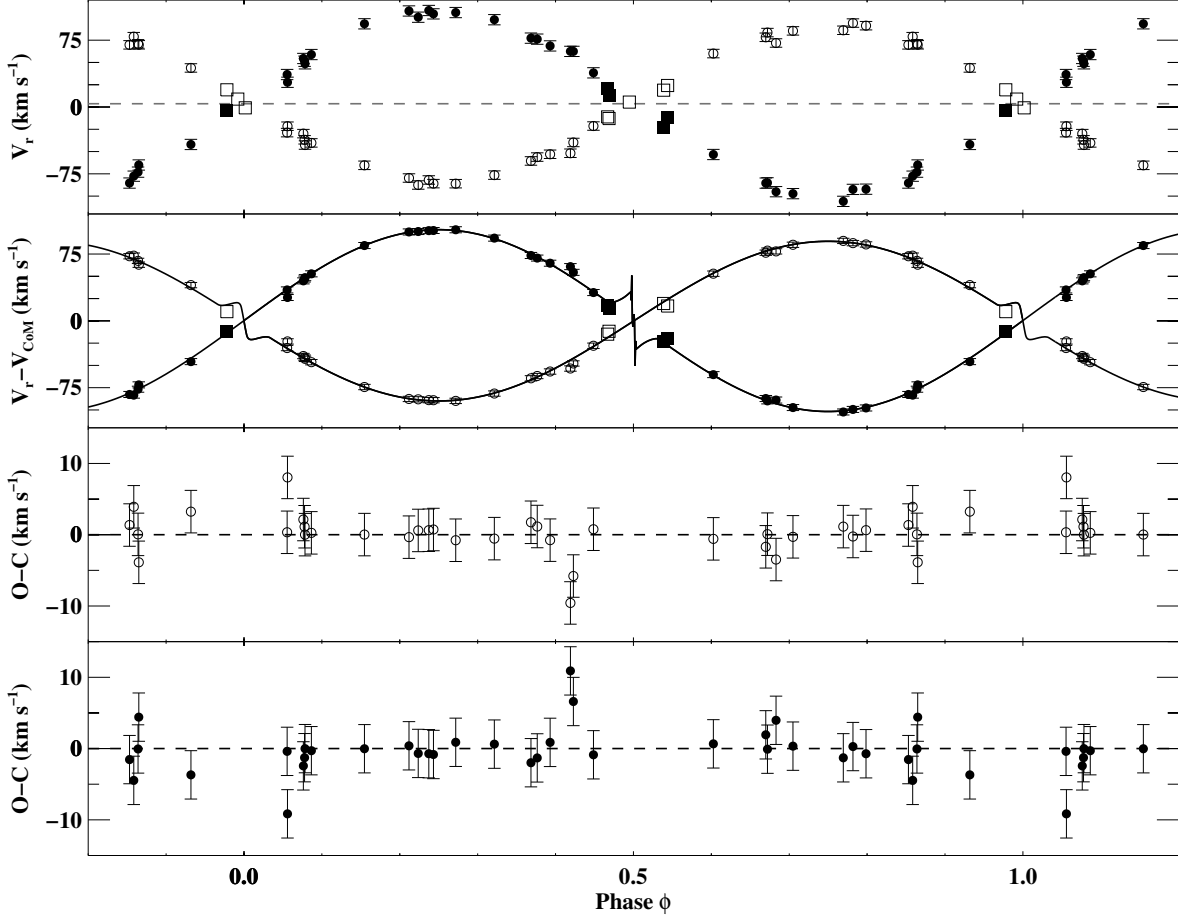


Fig. 5.— Radial-velocity observations for WOCS 40007 phased to the orbital period. The top panel shows the uncorrected RV data, while the second panel shows the RV data with the center-of-mass velocity variation due to the tertiary component removed. The black line in the second panel corresponds to the ELC model. The third and fourth panels show the $O - C$ diagrams for the eclipsing binary components. In all cases, open circles are primary star observations and filled circles are secondary. Open and filled squares are primary and secondary star observations that were not included in the ELC fit due to blending of the stellar spectra.

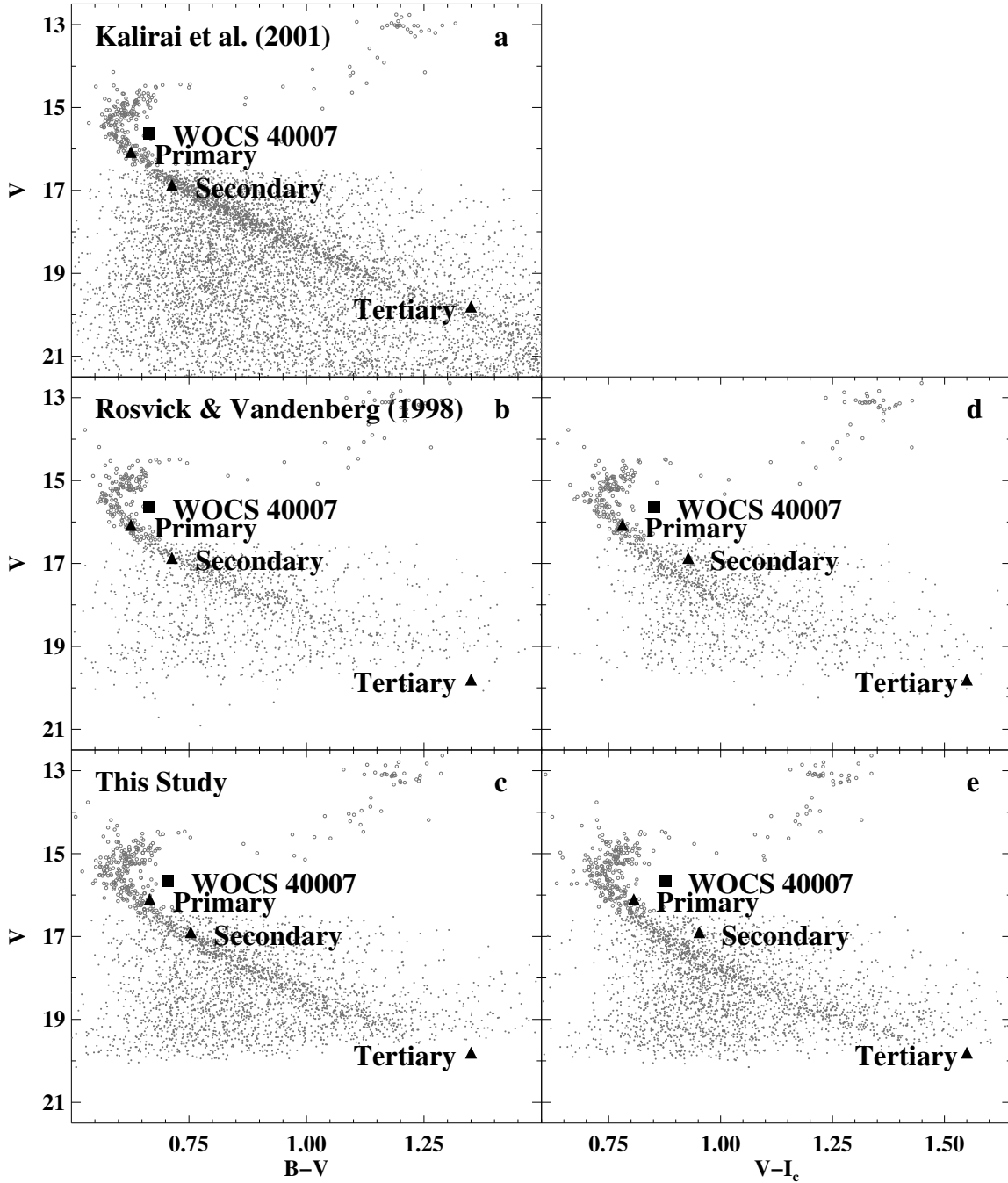


Fig. 6.— Derived locations of the DEB components in the CMD of NGC 6819 using the calibrated photometry of Kalirai et al. (2001, top panel), Rosvick & Vandenberg (1998, middle panel) and this study (bottom panel). The system photometry (squares), and that of the stellar components (triangles) are shown. Known cluster members are plotted as open circles for magnitudes brighter than the WOCS faint limit ($\lesssim 16.5$ mag).

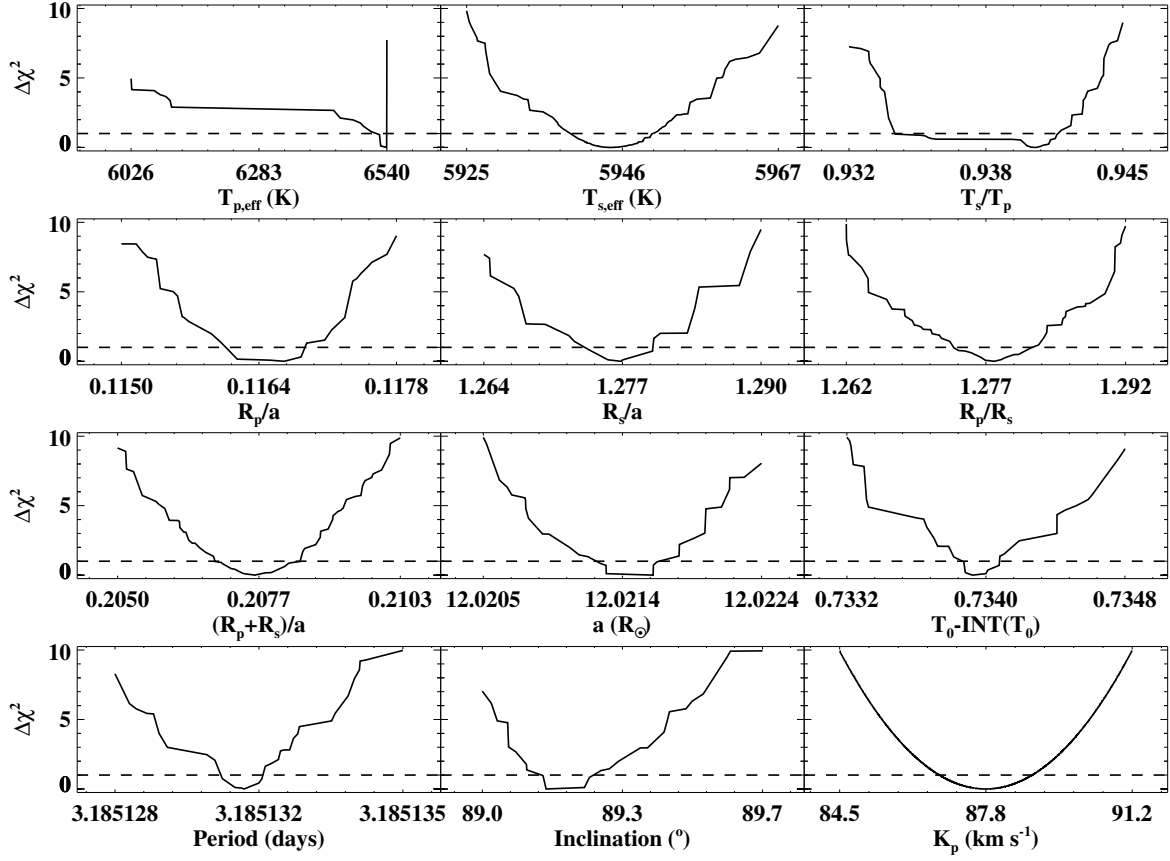


Fig. 7.— $\Delta\chi^2$ vs. fitted parameters for WOCS 40007. The solid line is the lower envelope of all models. The horizontal dashed line corresponds to $\Delta\chi^2 = 1$, representing the 1σ uncertainty in each parameter.

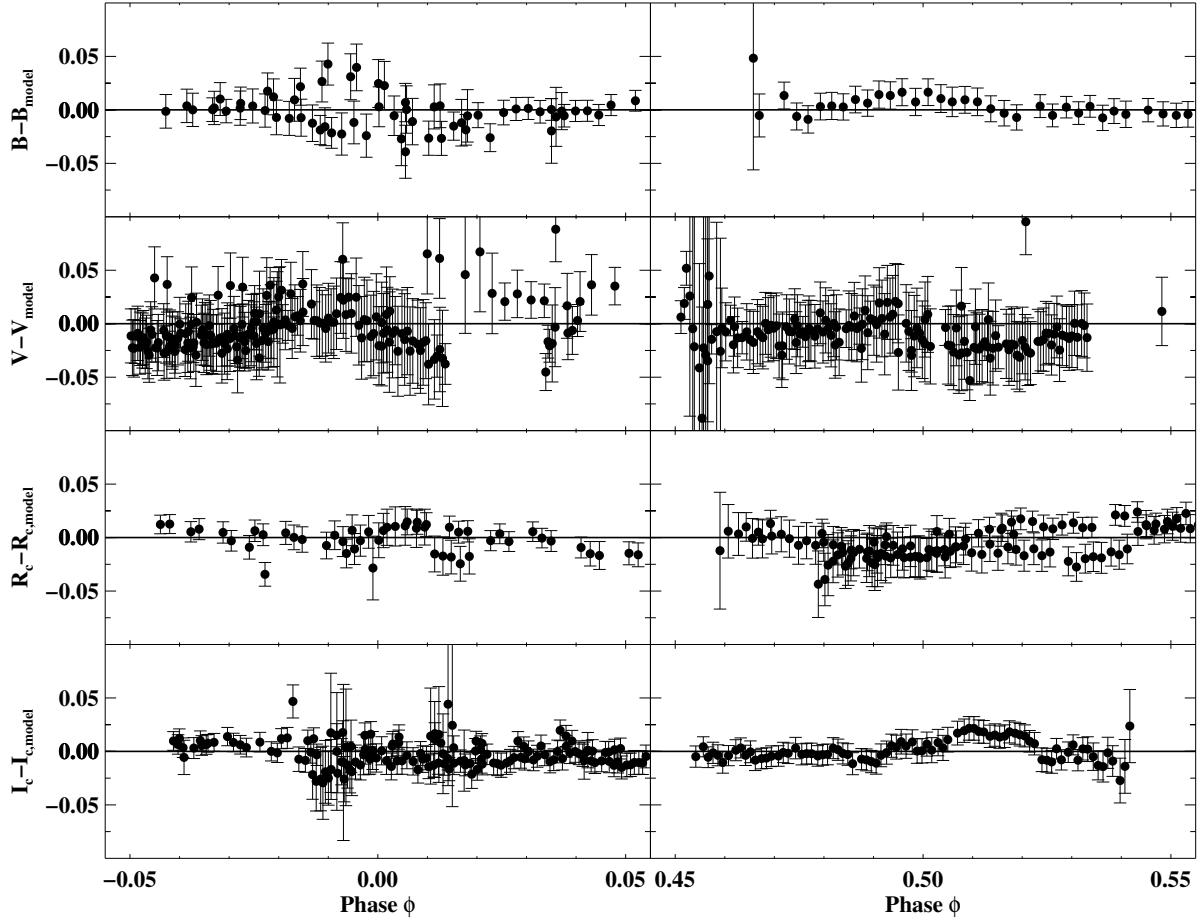


Fig. 8.— $O - C$ diagrams corresponding to the photometric solution presented in Figures 3 and 4, zoomed in on the primary (left column) and secondary (right column) eclipses. Data points included in this figure correspond to the data used by ELC to determine the best fit model.

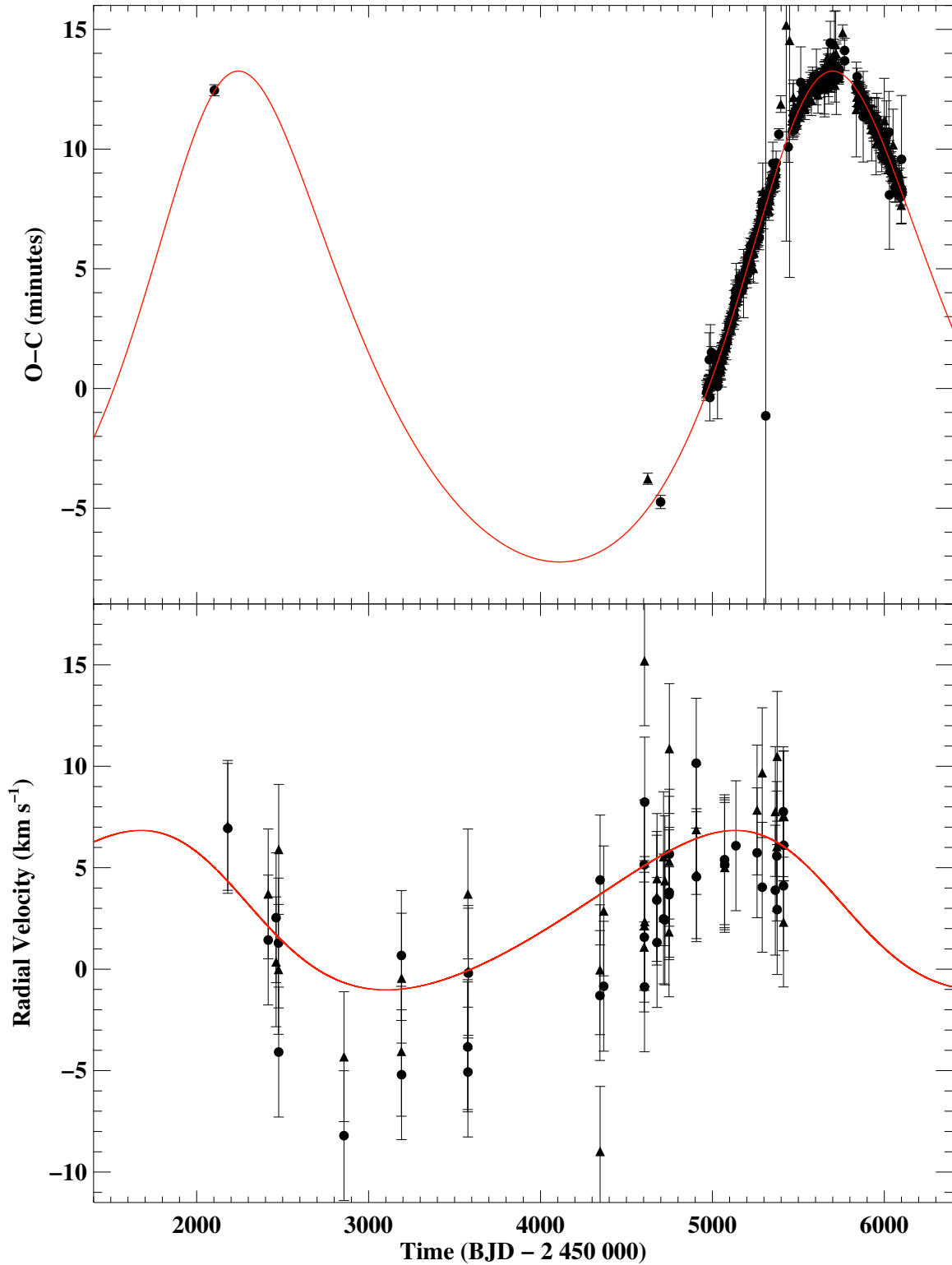


Fig. 9.— Observed minus computed values for primary (*solid dot*) and secondary (*solid triangle*) eclipse timing (*top panel*) and radial velocities of the barycenter as derived from the primary and secondary stars (*bottom panel*). The curves show the best fit from three-body models. The outliers in the eclipse timing panel are ground-based observations.

Table 4. Photometric and Spectroscopic Orbital Solutions of WOCS 40007

Parameter	Limb-Darkening Coefficients	Model Atmospheres
Constrained Parameters:		
e	0 (fixed)	0 (fixed)
q ($\mathcal{M}_2/\mathcal{M}_1$)	0.878 ± 0.009	0.878 ± 0.009
K_1 (km s^{-1})	89.6 ± 0.5	89.6 ± 0.5
K_2 (km s^{-1})	102.0 ± 0.6	102.0 ± 0.6
Free Parameters:		
P (d) ^a	3.1851308 ± 0.0000012	3.1851310 ± 0.0000018
t_0 (HJD – 2 450 000)	4698.7340 ± 0.0003	4698.7340 ± 0.0004
i ($^\circ$)	89.17 ± 0.12	88.81 ± 0.06
γ (km s^{-1}) ^b	0.62 ± 0.32	0.62 ± 0.32
\mathcal{R}_1/a	0.1164 ± 0.0006	0.1183 ± 0.0004
$\mathcal{R}_1/\mathcal{R}_2$	1.274 ± 0.006	1.293 ± 0.006
T_2/T_1	0.935 ± 0.007	0.936 ± 0.001
Derived Parameters:		
\mathcal{M}_1 (\mathcal{M}_\odot)	1.236 ± 0.020	1.236 ± 0.020
\mathcal{M}_2 (\mathcal{M}_\odot)	1.086 ± 0.018	1.086 ± 0.018
\mathcal{R}_1 (\mathcal{R}_\odot)	1.399 ± 0.007	1.423 ± 0.005
\mathcal{R}_2 (\mathcal{R}_\odot)	1.098 ± 0.004	1.100 ± 0.004
\mathcal{R}_2/a	0.0913 ± 0.0003	0.0915 ± 0.0003
$(\mathcal{R}_1 + \mathcal{R}_2)/a$	0.2078 ± 0.0007	0.2098 ± 0.0008
a (\mathcal{R}_\odot)	12.022 ± 0.001	12.023 ± 0.001
$\log g_1$ (cgs)	4.240 ± 0.005	4.226 ± 0.004
$\log g_2$ (cgs)	4.381 ± 0.004	4.379 ± 0.004
$v_{rot,1} \sin i$ (km s^{-1}) ^c	22.23 ± 0.11	22.61 ± 0.08
$v_{rot,2} \sin i$ (km s^{-1}) ^c	17.45 ± 0.07	17.48 ± 0.07

^aPeriod derived strictly from ground-based data, and is not corrected for effects of the tertiary star.

^bWe assume that the recessional velocity is identical for both components.

^cComputed assuming synchronism.

Table 5. Eclipse Timings for WOCS 40007

BJD-2450000	σ	Eclipse	Notes
2102.88906	0.00042	P	ground R_C
4623.88256	0.00024	S	ground V
4698.73159	0.00020	P	ground R_K
4964.69070	0.00025	S	start of Kepler Q1
4966.28308	0.00023	P	
4967.87586	0.00019	S	
4969.46819	0.00013	P	
4971.06104	0.00005	S	
4972.65339	0.00012	P	
4974.24608	0.00022	S	
4975.83853	0.00022	P	

Note. — This table is published in its entirety in the electronic edition, but a portion is shown here for guidance regarding its form and content.

Table 6. Orbit Solution for the Tertiary Star in WOCS 40007

Parameter	Value
P_b (d)	$3.18509876 \pm 0.00000007$
P_3 (d)	3547 ± 33
t_b	2452102.8797 ± 0.0001
t_3	2455613 ± 5
e_3	0.157 ± 0.002
ω_3 ($^\circ$)	77.0 ± 0.7
K_1 (km s $^{-1}$)	89.5 ± 0.7
K_2 (km s $^{-1}$)	101.9 ± 0.8
K_3 (km s $^{-1}$)	3.92 ± 0.03
γ (km s $^{-1}$)	0.62 ± 0.32
$q = \mathcal{M}_2/\mathcal{M}_1$	0.879 ± 0.010

Table 7. Age Estimates for NGC 6819

Model	CMD Isochrones	$M - R$ Diagram		
		WOCS 40007 Primary	WOCS 23009 Secondary	WOCS 23009
BaSTI	2.1	2.9 ± 0.5	3.4 ± 0.8	2.2 ± 0.2
DSEP	2.5	3.0 ± 0.5	3.3 ± 0.8	2.5 ± 0.2
VR	2.3	3.0 ± 0.5	3.4 ± 0.8	2.3 ± 0.2
Y ²	2.4	3.3 ± 0.5	3.7 ± 0.8	2.6 ± 0.2

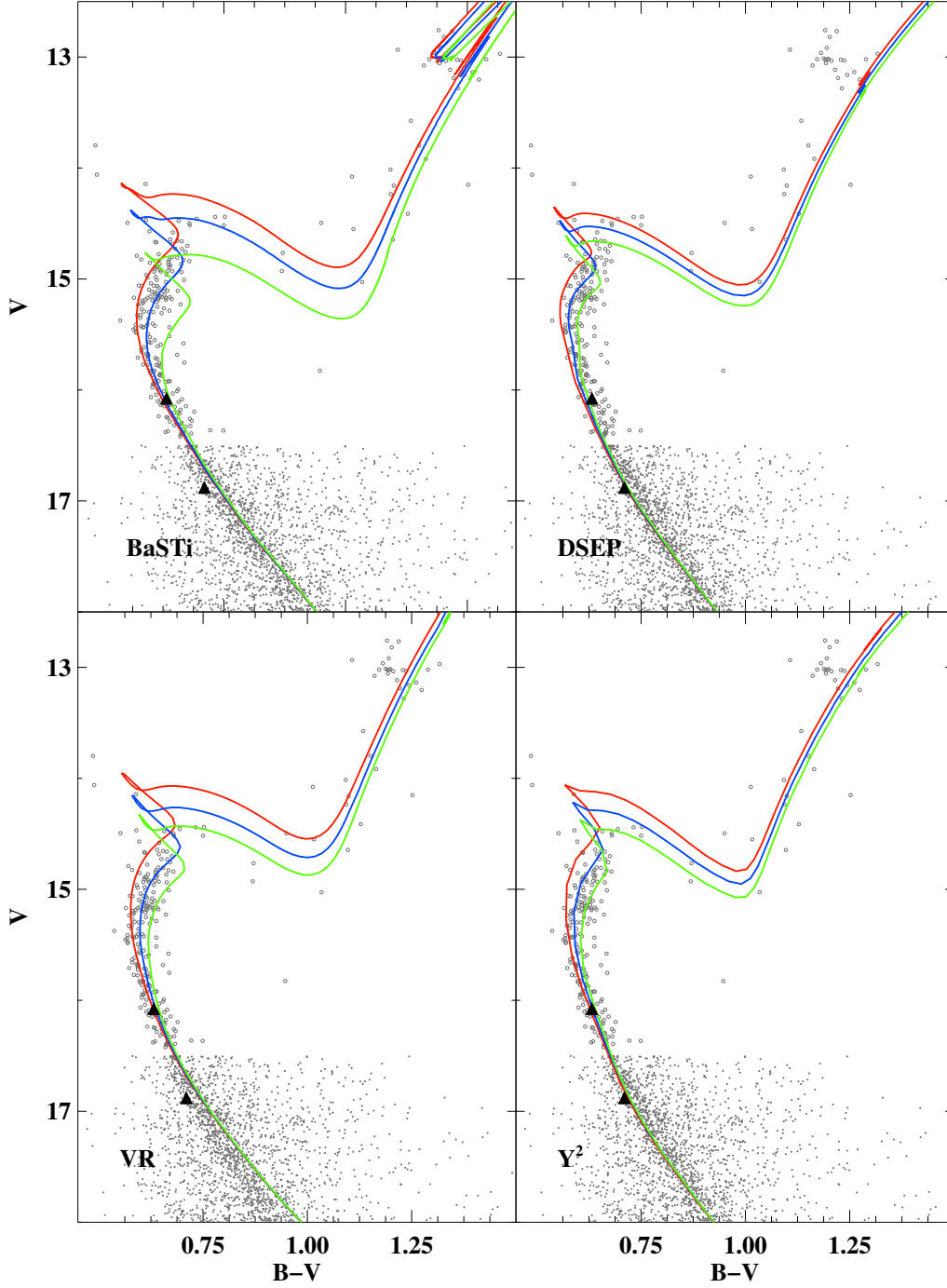


Fig. 10.— Color-magnitude diagram for NGC 6819 with 2.00, 2.25 and 2.50 Gyr isochrones for BaSTi, VR and Y^2 ; and 2.50, 2.75, and 3.00 Gyr isochrones for DSEP. Isochrones were shifted using our adopted reddening of $E(B - V) = 0.12$ and distance modulus $(m - M)_V = 12.30$. The decomposed photometry of the WOCS 40007 stars is shown as solid points. Kalirai et al. (2001) photometry is employed for the $(B - V, V)$ CMDs, while Talamantes et al. (2010) photometry is used for $(V - I, V)$.

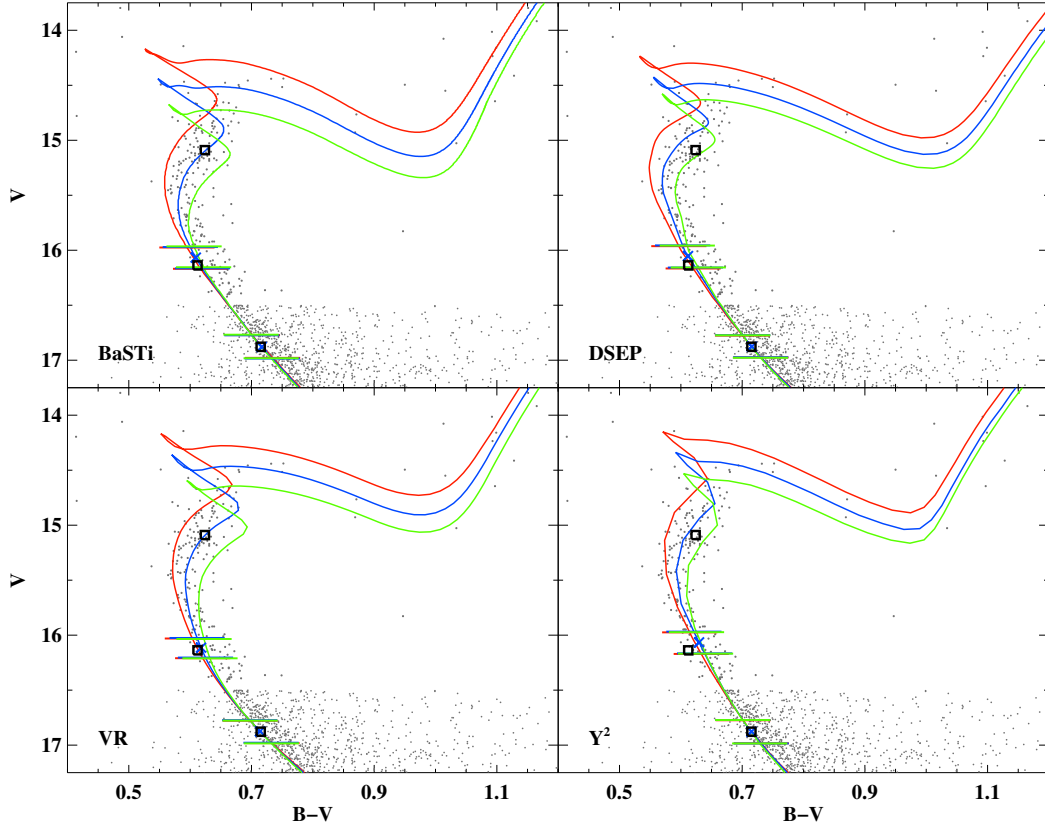


Fig. 11.— Color-magnitude diagram for NGC 6819 with isochrones shifted to fit the secondary star, as discussed in §5.1.1. We also include the primary component of WOCS 23009, as determined by Sandquist et al. (2013). Ages are 2.00, 2.25 and 2.50 Gyr for BaSTI isochrones; and 2.25, 2.50 and 2.75 Gyr for DSEP, VR, and Y^2 isochrones. Open squares show the decomposed photometry of WOCS 40007 stars from Kalirai et al. (2001) photometry, \times symbols mark the isochrone value for the measured mass of each component, and horizontal lines delimit the range covered 1σ mass uncertainties. Green lines correspond to the greatest age, blue to the middle, and red to the lowest age.

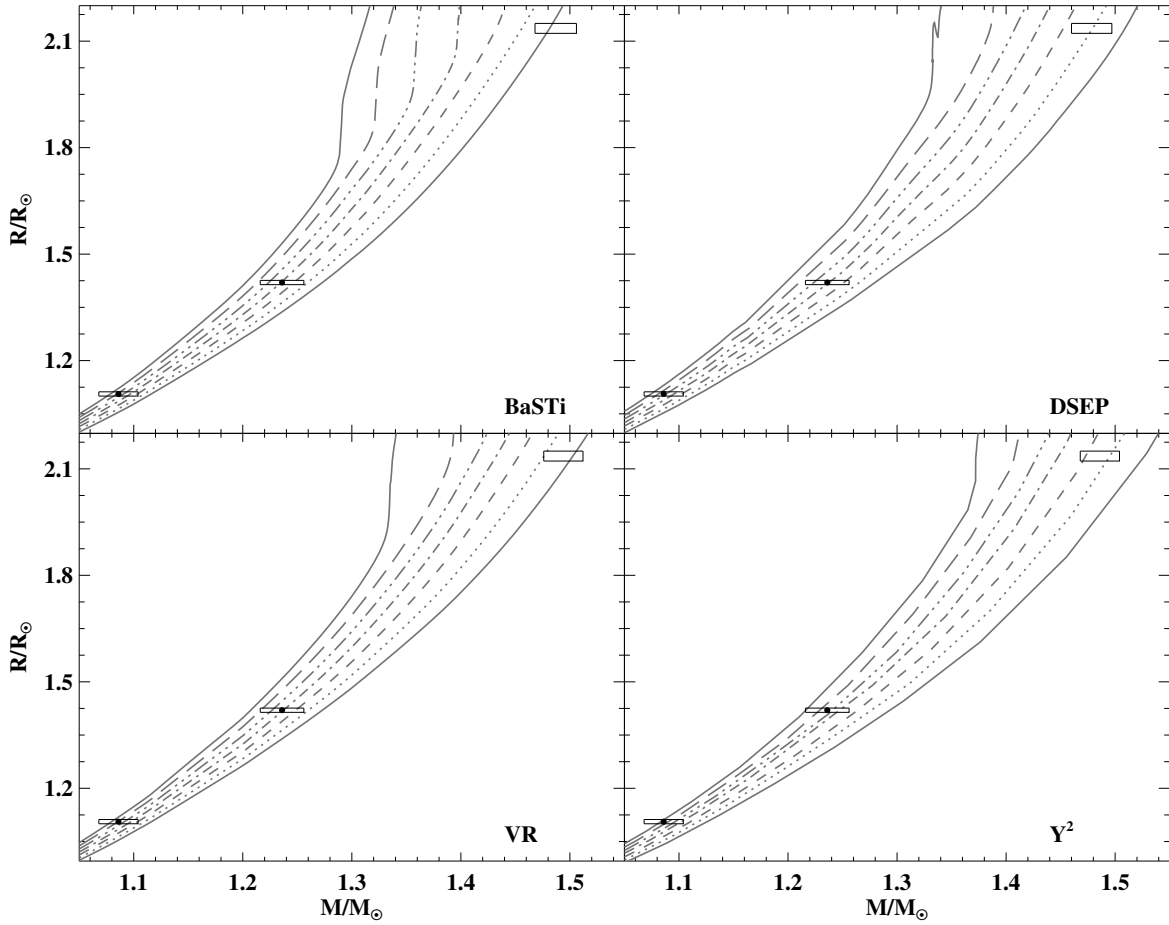


Fig. 12.— Derived masses and radii for the components of WOCs 40007 compared with the four isochrone sets. The isochrones employ metallicities of $[\text{Fe}/\text{H}] = +0.06, +0.09, +0.13$ and $+0.09$ for BaSTi, DSEP, VR and Y^2 models, respectively. Each panel has seven ages plotted and, from right to left, are: 2.25, 2.50, 2.75, 3.00, 3.25, 3.50, and 3.75 Gyr. The error boxes correspond to a 1σ uncertainty.

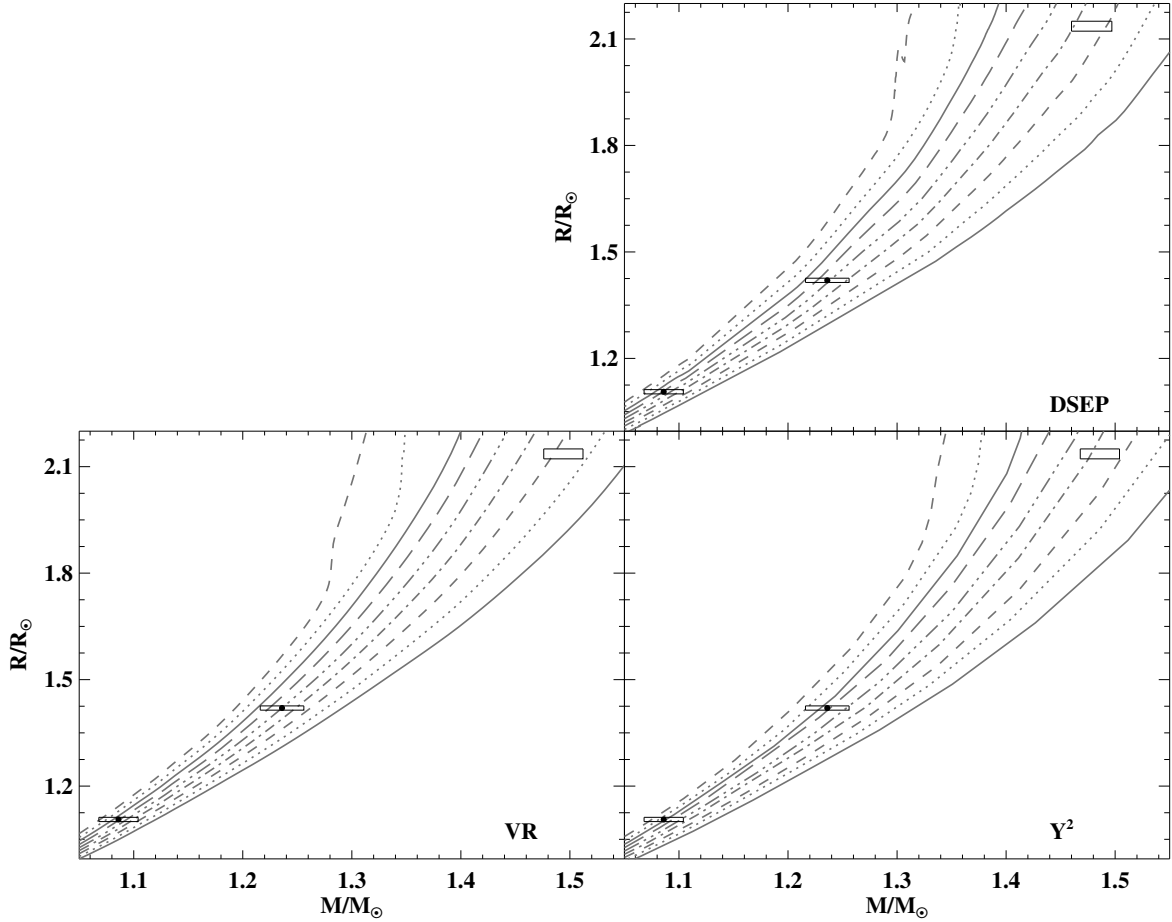


Fig. 13.— Derived masses and radii for the components of WOCS 40007 compared with three of the four isochrone sets. The isochrones were created with a decreased metallicity value of $[\text{Fe}/\text{H}] = -0.01, 0.00$ and -0.01 for DSEP, VR and Y², respectively. (BaSTI isochrones are not included because the tabulation does not include a closely matching metallicity value.) Each panel has nine ages plotted and, from right to left, are: 1.75, 2.00, 2.25, 2.50, 2.75, 3.00, 3.25, 3.50, and 3.75 Gyr. The error boxes correspond to a 1- σ uncertainty.

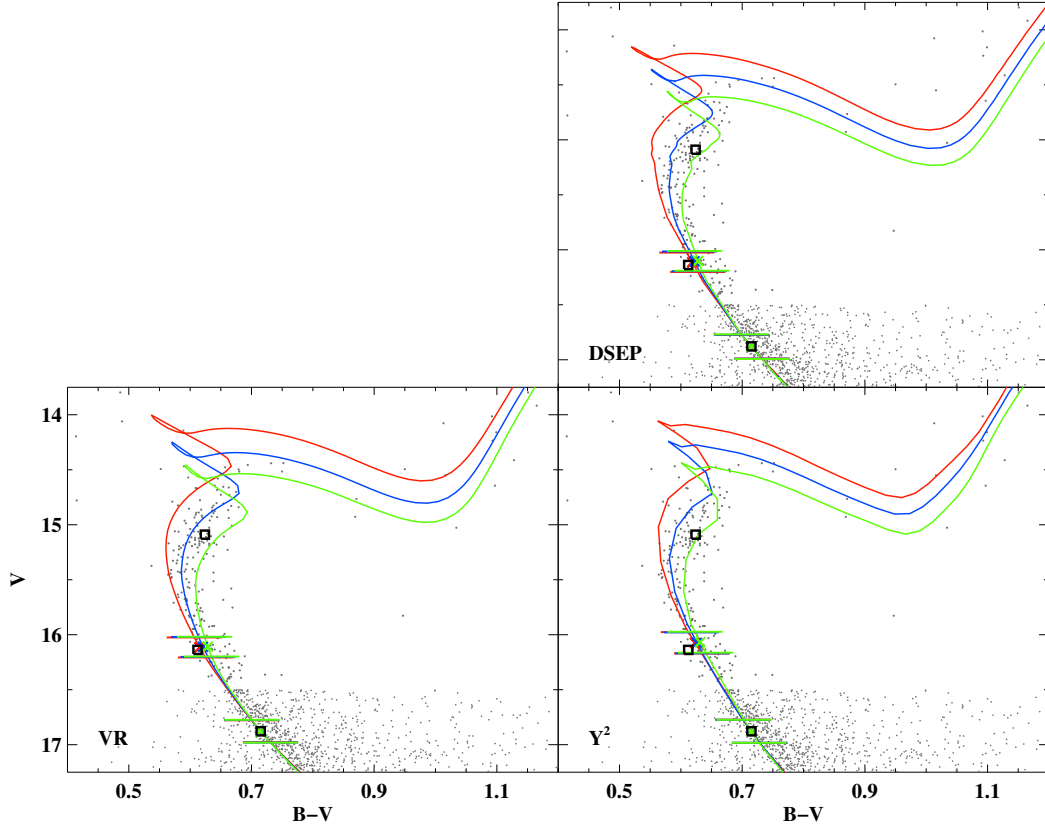


Fig. 14.— Color-magnitude diagram for NGC 6819 with 2.00, 2.25 and 2.50 Gyr isochrones for DSEP, VR and Y². Each isochrone set is plotted with a decreased metallicity value of $[\text{Fe}/\text{H}] = -0.01, 0.00,$ and -0.01 for DSEP, VR, and Y², respectively. (BaSTI isochrones are not included because the tabulation does not include a closely matching metallicity value.) All plotted points have the same definitions as in Figure 11.